# Proton exchange membrane water electrolysis: Modeling for hydrogen flow rate control

Rebah Maamouri, Damien Guilbert, Michel Zasadzinski, Hugues Rafaralahy

# Proton Exchange Membrane Water Electrolysis: Modeling for Hydrogen Flow Rate Control

Rebah Maamouri[(a)], Damien Guilbert[(a)], Michel Zasadzinski[(b)], and Hugues Rafaralahy[(b)]

(a) Université de Lorraine, GREEN, 54000 Nancy, France
(b) Université de Lorraine, CNRS, CRAN, 54000 Nancy, France

**Abstract**

Nowadays, the proton exchange membrane electrolyzer (PEMEL) is a promising and attractive technology when coupling with renewable energy sources (RES). Indeed, PEMEL can respond quickly to the dynamic operations of RES. Given that PEMEL must be supplied with a low DC voltage, DC-DC converters are mandatory. In this work, a stacked interleaved buck DC-DC converter is used. In this paper, the tuning of proportional, integral and derivative (PID) controllers, which are often used to enhance electrolyzer performances (efficient and reliable operation), is based on the dynamic behavior of the PEMEL. Before designing the PID controller, a model of the PEMEL is proposed based on input-output measured data, and this model is combined with the converter state-space description. Then, the obtained global model is used to tune two PID controller configurations: the first one to control the current and the second one to control the voltage of the PEMEL. Experimental tests are carried out to validate the effectiveness of the designed control laws.

**Keywords** PEM water electrolysis; stacked interleaved buck DC-DC converter; modeling; PID controller.

## 1 Introduction

Increasing requirements to reduce pollutant emissions and excessive natural energy sources consumption have inspired innovation in the field of clean energy sources. Among clean energy sources, fuel cells are regarded as one of the most promising technologies, due to their reliability, compactness, and efficiency [1]. A fuel cell is an electrochemical device that generates electricity from hydrogen and oxygen. Hydrogen can be provided from water electrolysis, which is considered the cleanest production system especially when the electrolysis units are supplied by renewable energy sources (RES) [2]. The produced hydrogen can be combined with power generation equipment including fuel cells and can also be used for a variety of applications, including industrial processes, vehicle fueling, and injection into natural gas pipelines [3, 4].

Different electrolysis technologies are used to produce hydrogen and are distinguished by their electrolytes and the charge carrier: alkaline electrolyzer, proton exchange membrane electrolyzer (PEMEL), and solid oxide electrolyzer [5, 6, 7]. Among these technologies, alkaline electrolysis is at its mature stage, however, several enhancements such as working pressure and current density still should be made [8]. The PEMEL is in the pre-commercial stage for laboratory research purposes and small-scale applications [9]. For this technology, researches are mainly focused on reducing the cost of catalysts and stack components, and on its integration with RES [9, 10]. Solid oxide electrolysis technology attracted a great deal of interest in the 1980s, but it is still under development and not yet commercialized [11]. Current research activities are focused on the development of new materials with good high-temperature stability.

e-mails: rebah.maamouri@univ-lorraine.fr, damien.guilbert@univ-lorraine.fr, michel.zasadzinski@univ-lorraine.fr, hugues.rafaralahy@univ-lorraine.fr.

Published in Internationall Journal of Hydrogen Energy, 2021, vol. 46, iss. 11, pp. 7676-7700.

Comparative studies presenting the main features and the advantages and disadvantages of each technology have been realized in [6, 7, 12]. These studies show that PEMELs present numerous advantages over alkaline electrolysis technology, such as compactness, relatively simple system design, fast system response and ability to operate in safety at higher current densities. Therefore, PEMEL technology offers an interesting option to be safely integrated into a hydrogen-based production energy network and is considered in this work.

When considering an electrolyzer integrated with a hydrogen production system based on RES, it must be connected with a power conditioning system. Usually, a DC-DC converter is required to couple the PEMEL to the RES. Given that the PEMEL requires a low rated voltage (roughly equal to 8 V [13]) to maximize the production of hydrogen from water electrolysis, DC-DC buck converters are commonly used for this purpose [14, 15, 16]. However, depending on the electrical grid and the feature of the PEMEL, different DC-DC converter topologies can be employed [13, 17].

Recently, several DC-DC converter topologies have been proposed for PEMEL applications and recent research works have been reported in the literature regarding the analysis of their advantages and drawbacks [18, 19, 20, 21, 22, 23, 24, 25, 26, 27, 28, 29]. In these applications, DC-DC converters must respond to several challenging issues other than output current ripples, especially in terms of voltage ratio, cost, energy efficiency and reliability in case of power switch failures. A detailed literature review that has been carried out in [17] shows that the classic buck converter topology does not meet several requirements, especially in terms of reliability (one single switch fault), efficiency and voltage ratio. Most articles dealing with DC-DC converters and their controls for electrolyzer applications include only simulation results [14, 15, 16, 29]. Therefore, new contributions including experiments with electrolyzers are required to assess the performance of developed DC-DC converters and their control.

Starting from this comparison study, interleaved DC-DC converter topologies have gained growing interest from researchers and industrials due to their benefits, particularly in terms of energy efficiency optimization, current ripple reduction, and availability in case of failures [30, 31]. In [29], a sliding mode controller has been developed for an interleaved buck converter supplying a PEMEL, but only simulation results are presented. By comparison, in [32], the authors have developed a proportional and integral (PI) controller to regulate the stack voltage of a PEMEL coupled with a three-level interleaved buck converter. Experimental results are presented to validate the proposed control strategy.

Since the current ripple reduction is one of the most important features requested for PEMEL, a stacked interleaved DC-DC buck converter (SIBC) has been considered for this work. Previous works employing the SIBC converter for PEMEL applications have been developed in the literature. In [33], the authors have developed a gain scheduling PI controller combined with a feedforward action to regulate the current of the PEMEL. The current to regulate has been chosen to optimize the efficiency of the whole SIBC-PEMEL. By comparison, in [34], the authors have developed a PI controller combined with a feedforward action to control the stack voltage of the PEMEL. The stack voltage to regulate has been chosen to maximize the hydrogen flow rate. In both works, experiments have been performed to confirm the effectiveness of the control.

The main objective of this work is to design industrial control laws for PEMEL. Since proportional, integral and derivative (PID) controllers are the most used in industrial applications, this type of compensator has been considered. For control purposes, modeling of the PEMEL is needed. So a dynamic model of the PEMEL is determined by using a least-square approach with input-output measured data (current-voltage). This modeling approach differs from that introduced in [35] where the parameters of the dynamic model are determined by a static and dynamic characterization. The obtained discrete-time model is transformed into a continuous one. By employing the state-space averaging approach given in [36, 37], a state-space model of the overall PEMEL-SIBC is determined and used to design the PID control laws. Two cases have been considered: the controlled output is either the current or the voltage of the PEMEL.

The outline of this paper is the following. After presenting motivations to carry out this work, Section 2 deeply investigates the PEMEL modeling and particular attention is given to PEMEL dynamic behavior. Section 3 is dedicated to the determination of the state-space average model of the overall PEMEL-SIBC. The design of the PID controllers is described in Section 4. Finally, the effectiveness of the designed control laws is validated on an experimental test bench in Section 5.

## 2 PEM electrolyzer modeling

PEMEL is considered as a load and an accurate model must be taken into consideration to develop efficient controllers. Indeed, the modeling of the load may have an impact on the design and tuning of the controller. Besides, modeling is mandatory to test the effectiveness and performance of the controller in simulations including the DC-DC converter connected to a PEMEL model. As a result, simulations results allow providing crucial information about the dynamic performance of the electrolyzer experimentally, since an accurate model has been taken into consideration to replicate its operation.

In the literature, different models of PEMEL have been developed. In [14, 15, 16, 18, 19, 20, 32, 38, 39], the electrolyzer can be modeled as a simple resistor; whereas in [40, 41, 42, 43], it is modeled by an equivalent circuit composed of a resistance series connected to a voltage generator representing the reversible voltage. In the major part of these papers and articles, too few information is provided regarding the determination of the parameters of the model. Static models are useful when the PEMEL operates in static conditions, but they are not suitable when the PEMEL has to operate under dynamic operations (i.e. when the PEMEL is coupled with RES).

Besides, dynamic modeling has been introduced in other related works [44, 45, 46], In [44], the authors have introduced a dynamic model inspired by previous works developed for fuel cells. Experiments have been performed to show the dynamics of a single-cell PEMEL but the authors have not assessed the parameters of the equivalent circuit from experimental data. In comparison, in [45], the same model is reported based on [44]. However, a static model is employed to be connected with an interleaved DC-DC buck converter for control purposes. Then, in [46], this model is used for an alkaline electrolyzer to analyze the consequences of rectifiers on the specific energy consumption and gas quality during dynamic operation. Finally, in [35], a dynamic model has been introduced from experimental tests and knowledge on fuel cell modeling. The parameters of the model have been evaluated based on a static and dynamic characterization by using a sample of data for a specific current range.

The dynamic operations of the electrolyzer have an impact on the dynamic behavior of the whole converter-electrolyzer. For this reason, it has been decided to investigate the dynamic operation of the electrolyzer. The objective is therefore to develop a dynamic model of the electrolyzer and to determine the parameters of the model. The retained model is a transfer function with the measured current (called $i_{e\ell}$) as input and the measured stack voltage (called $v_{e\ell}$) as output. In addition, it is useful to have a dynamic model of the electrolyzer during the synthesis of a control law because it is necessary not only to control the converter but also the whole converter-electrolyzer. Then, the design a PID controller for the electrolyzer is based on three steps as follows:

**1)** The PEMEL without the SIBC is modeled by a transfer function by using a black box approach based on current and voltage measurements, without using physical laws. In Section 2.1, the measured data of the PEMEL are given. To obtain a continuous-time model from the sampled measurements, a procedure into three steps is detailed in Section 2.2.
   - **a)** A least-square method is used to estimate the parameters of a discrete-time model using the sampled measured data.
   - **b)** The bilinear transform is applied on the discrete-time model to obtain a continuous-time one.
   - **c)** Since the order of the continuous-time transfer function can be unnecessarily high, a balanced truncation is then applied to the obtained transfer function with a low order.

**2)** Using the well-known state-space averaging techniques given in [36, 37], the state-space realization of the whole SIBC-PEMEL is provided in Section 3.

**3)** By using the SIBC-PEMEL model obtained in the previous step, two PID controllers are designed in Section 4 and tested on the experimental bench in closed loop in Section 5.

### 2.1 Investigations of the dynamic operations

To analyze the dynamic operation of the studied PEMEL NMH2 1000 from Heliocentris Company in which the features are provided in Table 1, a fit experimental test rig has been realized at the GREEN laboratory as shown in Figure 1. The realized experimental test rig is described in the caption of Figure

1. The current $i_{e\ell}$ and voltage $v_{e\ell}$ of the PEMEL are acquired respectively by a current clamp PAC 12 from Chauvin Arnoux Company and by a voltage differential probe from Chauvin Arnoux Company. Since it is a commercial electrolyzer including power electronics for education purposes, only the stack of the electrolyzer is employed in our work.

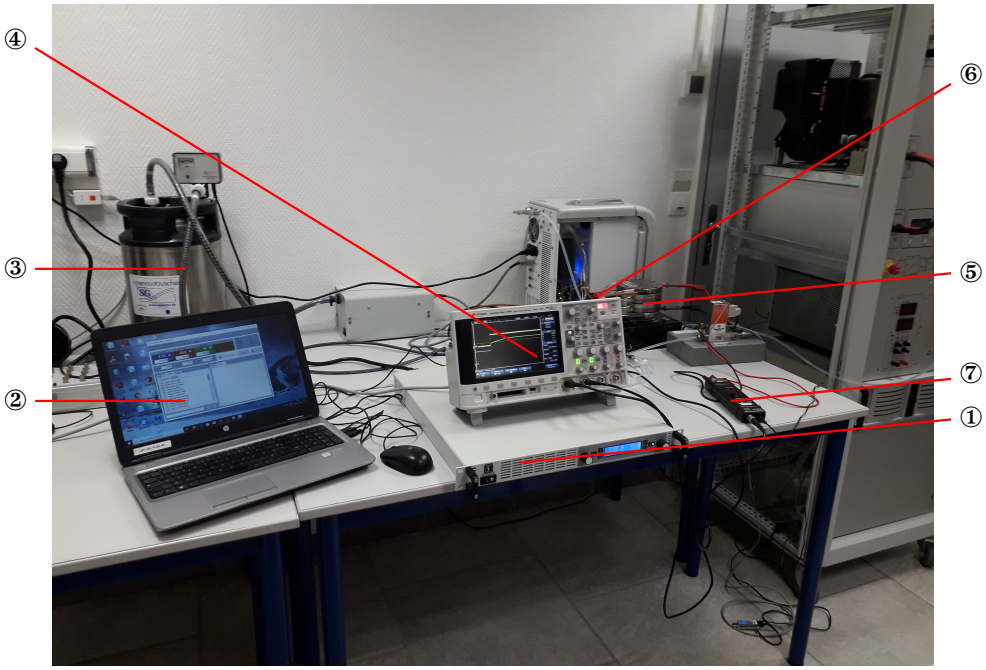


Figure 1: Experimental test bench of the PEM electrolyzer: ① → controlled DC power supply, ② → virtual control panel with a laptop, ③ → pressurized pure water tank, ④ → 4-channel oscilloscope, ⑤ → PEMEL, ⑥ → a current clamp, ⑦ → voltage probe.

Table 1: Features of the PEM electrolyzer.

| **Parameters** | **Values** | **Units** |
|---|---|---|
| Rated electrical power | 400 | W |
| Stack operating voltage | 8 | V |
| Stack current range | 0-50 | A |
| $H_2$ output pressure | 10.5 | bar |
| Cells number, $N$ | 3 | – |
| Active area section | 50 | $cm^2$ |
| Rated hydrogen flow rate at STP (Standard Temperature and Pressure, 20°C and 1 bar) | 1 | slpm (standard liter per minute) $P = 1$ bar $T = 15$°C |

A continuous-time transfer function $F_h(s)$ is considered as model in the following general form for the PEMEL

$$F_h(s) = \frac{V_{e\ell}(s)}{I_{e\ell}(s)} = \frac{b_{n_r} s^{n_r} + b_{n_r-1} s^{n_r-1} + \ldots + b_1 s + b_0}{s^{n_r} + a_{n_r-1} s^{n_r-1} + \ldots + a_1 s + a_0} \tag{1}$$

where $V_{e\ell}(s)$ and $I_{e\ell}(s)$ are the Laplace transforms of $v_{e\ell}(t)$ and $i_{e\ell}(t)$, respectively.

The block diagram in Figure 2 allows to show the relationship between the experimental test bench of the PEM electrolyzer in Figure 1 and $F_h(s)$.

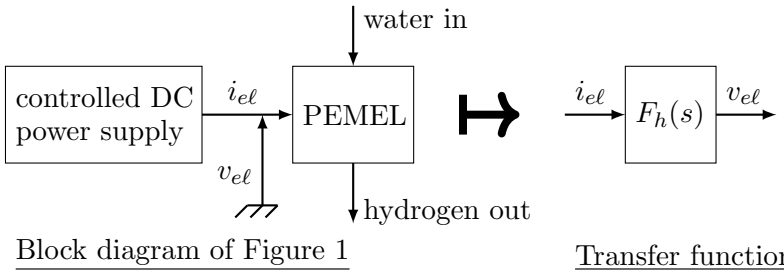


Figure 2: Relationship between the experimental test bench of the PEM electrolyzer in Figure 1 and the transfer function $F_h(s)$ in (1).

To determine the coefficients of the continuous-time model $F_h(s)$ given in (1), a step current $i_{e\ell}$ is applied to the PEMEL shown in Figure 1 and a voltage response $v_{e\ell}$ is obtained. The sampled measurements of the current $i_{e\ell}$ and the voltage $v_{e\ell}$ are given in Figure 3.

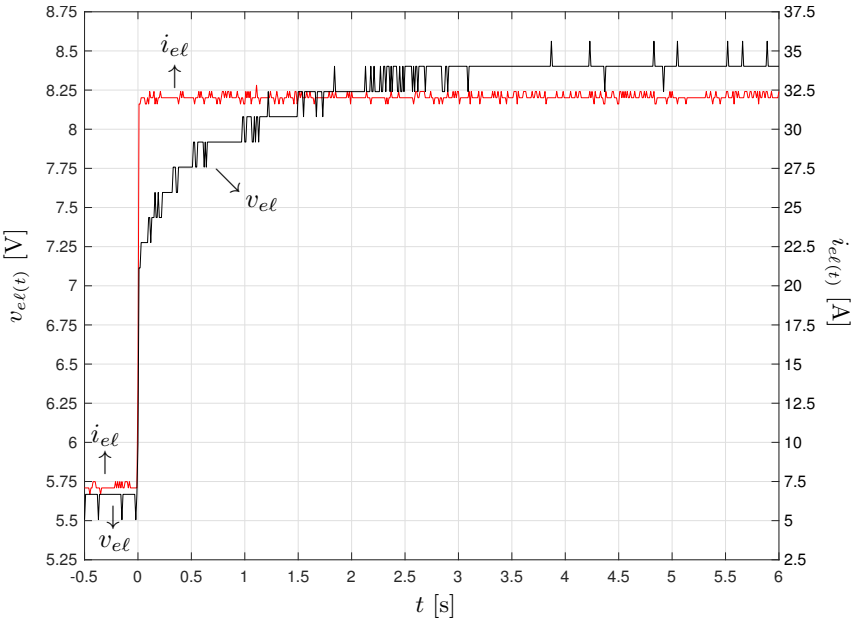


Figure 3: PEM electrolyzer: input current $i_{e\ell}$ and output voltage $v_{e\ell}$.

The sample time interval using to obtain Figure 3 is $T_s = 0.01$ s and the number of available samplings is $\mathcal{N} = 651$.

The step current is applied at $t = 0$ s. Before applying the step current, the value of the stack voltage $v_{e\ell}$ is equal to the sum of the reversible voltage (i.e. open-circuit voltage), and activation and ohmic overvoltage as well. As a result of the step current, an instantaneous increase of the stack voltage, and then a slow increase can be noticed before reaching a steady-state operation at $t = 3$ s. The instantaneous increase in stack voltage corresponds to the ohmic overvoltage since the electrolyte of the electrolyzer can be modeled as a simple resistor and does not include any dynamics [35]. In comparison, the slow increase in stack voltage represents the chemical reactions both at the anode and the cathode [35].

In this experiment, this final rise lasts 3 s and its length can vary (shorter or longer) according to the operating conditions (initial stack voltage, step current). Indeed, as highlighted in [35], the duration of the final rise before reaching the steady-state operation due to the reaction kinetics into the anode and cathode lengthens especially as the input energy increases. However, when the stack voltage gets closer to the limit operating voltage (for this PEMEL, the limit voltage is equal to 8 V, corresponding to the rated stack voltage), the dynamics are faster (as reported in Figure 3). In this work, this set of data is used to accurately determine the model and its parameters. Since the parameters may change according to the operating conditions, the same operating conditions (as reported in Figure 3) are kept to validate the effectiveness of the proposed controller by simulations and experiments. To summarize, this slow rise represents the activation overvoltage both at the anode and cathode.

The next subsection is focused on the determination of the parameters of this model. Then, this model is validated by comparing it with the experiments shown in Figure 3. Finally, the obtained results are discussed based on previous research works on PEMEL modeling in Subsection 2.3.

## 2.2 Determination of a transfer function to model the dynamic behavior of the PEM electrolyzer

To obtain the coefficients of the transfer function given in (1) using the experimental response of the PEMEL given in Figure 3, we proceed in three steps.

**1)** A least-square approach is used to find a discrete-time transfer function $\overline{F}_h(z)$ of order $n$ given by

$$\overline{F}_h(z) = \frac{\overline{b}_n z^n + \overline{b}_{n-1} z^{n-1} + \ldots + \overline{b}_1 z + \overline{b}_0}{z^n + \overline{a}_{n-1} z^{n-1} + \ldots + \overline{a}_1 z + \overline{a}_0} \tag{2}$$

such that the output obtained by injecting the measured current $i_{e\ell_k}$ in the filter $\overline{F}_h(z)$ approximates the measured voltage $v_{e\ell_k}$ at best, where $k$ is the number of the sample at sample time $kT_s$.

**2)** A continuous-time model $\widetilde{F}_h(s)$ is computed by using the bilinear transform as follows

$$\widetilde{F}_h(s) = \overline{F}_h(z)\big|_{s=\frac{2}{T_s}\frac{z-1}{z+1}}\,. \tag{3}$$

**3)** The transfer function $F_h(s)$ of order $n_r < n$, defined in (1), is obtained by means of a balanced truncation proposed by Moore in [47] on the system $\widetilde{F}_h(s)$.

1st step: obtention of a discrete-time model $\overline{F}_h(z)$.

Let $\overline{N}_h(z)$ and $\overline{D}_h(z)$ be the numerator and the denominator of $\overline{F}_h(z)$ in (2). Let $\varepsilon_k$ be the modeling error made when the model $\overline{F}_h(z)$, defined in (2), is used. Then, the relationship between the measured values of $i_{e\ell}$ and $v_{e\ell}$ shown in Figure 3 can be written as follows

$$V_{e\ell}(z) = \frac{\overline{N}_h(z)}{\overline{D}_h(z)} I_{e\ell}(z) + \frac{1}{\overline{D}_h(z)} \mathcal{E}(z) \tag{4}$$

where $V_{e\ell}(z)$, $I_{e\ell}(z)$ and $\mathcal{E}(z)$ are the $\mathcal{Z}$ transforms of discrete-time signals $v_{e\ell_k}$, $i_{e\ell_k}$ and $\varepsilon_k$, respectively ($k$ is the sample number at the time sample $kT_s$).

Rewriting relation (4) in the time domain gives the following recurrence equation

$$v_{e\ell_k} = \sum_{j=0}^{n} \overline{b}_j i_{e\ell_{k-n+j}} - \sum_{j=0}^{n-1} \overline{a}_j v_{e\ell_{k-n+j}} + \varepsilon_k. \tag{5}$$

With $k = n, \ldots, \mathcal{N}$, equation (5) can be written in the following matrix form

$$Y_{\mathcal{N}} = \Phi_{\mathcal{N}} \theta + \mathcal{E}_{\mathcal{N}}, \tag{6}$$

where

$$Y_{\mathcal{N}} = \begin{bmatrix} v_{e\ell_n} \\ v_{e\ell_{n+1}} \\ v_{e\ell_{n+2}} \\ \vdots \\ v_{e\ell_{\mathcal{N}-1}} \\ v_{e\ell_{\mathcal{N}}} \end{bmatrix},\ \theta = \begin{bmatrix} \overline{b}_n \\ \overline{b}_{n-1} \\ \vdots \\ \overline{b}_1 \\ \overline{b}_0 \\ \overline{a}_{n-1} \\ \overline{a}_{n-2} \\ \vdots \\ \overline{a}_1 \\ \overline{a}_0 \end{bmatrix},\ \mathcal{E}_{\mathcal{N}} = \begin{bmatrix} \varepsilon_n \\ \varepsilon_{n+1} \\ \varepsilon_{n+2} \\ \vdots \\ \varepsilon_{\mathcal{N}-1} \\ \varepsilon_{\mathcal{N}} \end{bmatrix},$$

$$\Phi_N = \begin{bmatrix} i_{e\ell_n} & i_{e\ell_{n-1}} & \cdots & i_{e\ell_1} & i_{e\ell_0} & -v_{e\ell_{n-1}} & -v_{e\ell_{n-2}} & \cdots & -v_{e\ell_1} & -v_{e\ell_0} \\ i_{e\ell_{n+1}} & i_{e\ell_n} & \cdots & i_{e\ell_2} & i_{e\ell_1} & -v_{e\ell_n} & -v_{e\ell_{n-1}} & \cdots & -v_{e\ell_2} & -v_{e\ell_1} \\ i_{e\ell_{n+2}} & i_{e\ell_{n+1}} & \cdots & i_{e\ell_3} & i_{e\ell_2} & -v_{e\ell_{n+1}} & -v_{e\ell_n} & \cdots & -v_{e\ell_3} & -v_{e\ell_2} \\ \vdots & \vdots & \vdots & \vdots & \vdots & \vdots & \vdots & \vdots & \vdots & \vdots \\ i_{e\ell_{\mathcal{N}-1}} & i_{e\ell_{\mathcal{N}-2}} & \cdots & i_{e\ell_{\mathcal{N}-n}} & i_{e\ell_{\mathcal{N}-n-1}} & -v_{e\ell_{\mathcal{N}-2}} & -v_{e\ell_{\mathcal{N}-1}} & \cdots & -v_{e\ell_{\mathcal{N}-n}} & -v_{e\ell_{\mathcal{N}-n-1}} \\ i_{e\ell_{\mathcal{N}}} & i_{e\ell_{\mathcal{N}-1}} & \cdots & i_{e\ell_{\mathcal{N}-n+1}} & i_{e\ell_{\mathcal{N}-n}} & -v_{e\ell_{\mathcal{N}-1}} & -v_{e\ell_{\mathcal{N}-2}} & \cdots & -v_{e\ell_{\mathcal{N}-n+1}} & -v_{e\ell_{\mathcal{N}-n}} \end{bmatrix}.$$

The least-squares method consists of estimating $\theta$ by minimizing the square of the norm of $\mathcal{E}_{\mathcal{N}}$ given by

$$\begin{aligned} \|\mathcal{E}_{\mathcal{N}}\|^2 &= \mathcal{E}_{\mathcal{N}}^T \mathcal{E}_{\mathcal{N}} = (Y_{\mathcal{N}} - \Phi_{\mathcal{N}}\theta)^T (Y_{\mathcal{N}} - \Phi_{\mathcal{N}}\theta) \\ &= Y_{\mathcal{N}}^T Y_{\mathcal{N}} - Y_{\mathcal{N}}^T \Phi_{\mathcal{N}}\theta - \theta^T \Phi_{\mathcal{N}}^T Y_{\mathcal{N}} + \theta^T \Phi_{\mathcal{N}}^T \Phi_{\mathcal{N}}\theta. \end{aligned} \tag{7}$$

$\|\mathcal{E}_{\mathcal{N}}\|^2$ is minimal if

$$0 = \frac{\mathrm{d}\|\mathcal{E}_{\mathcal{N}}\|^2}{\mathrm{d}\theta} = 2\Phi_{\mathcal{N}}^T \Phi_{\mathcal{N}}\theta - 2\Phi_{\mathcal{N}}^T Y_{\mathcal{N}}, \tag{8}$$

and the optimal value of $\theta$ is $\widehat{\theta}$ given by

$$\widehat{\theta} = \left(\Phi_{\mathcal{N}}^T \Phi_{\mathcal{N}}\right)^{-1} \Phi_{\mathcal{N}}^T Y_{\mathcal{N}}. \tag{9}$$

The above procedure is applied to estimate the coefficient of the discrete-time transfer function $\overline{F}_h(z)$ in (2) with orders $n = 1$, $n = 2$, $n = 5$ and $n = 8$. The obtained results are given in Table 2.

Table 2: Estimation of the coefficients of $\overline{F}_h(z)$.

| $n$ | 1 | 2 | 5 | 8 |
|---|---|---|---|---|
| $\overline{b}_8$ | × | × | × | 0.056665 |
| $\overline{b}_7$ | × | × | × | −0.0070842 |
| $\overline{b}_6$ | × | × | × | 0.00076362 |
| $\overline{b}_5$ | × | × | 0.056568 | −0.013993 |
| $\overline{b}_4$ | × | × | −0.010708 | −0.0021986 |
| $\overline{b}_3$ | × | × | −0.0022945 | −0.0092568 |
| $\overline{b}_2$ | × | 0.055779 | −0.018961 | −0.0078828 |
| $\overline{b}_1$ | 0.055152 | −0.026472 | −0.0055832 | −0.0055324 |
| $\overline{b}_0$ | −0.050386 | −0.025226 | −0.014342 | −0.0053431 |
| $\overline{a}_7$ | × | × | × | −0.17929 |
| $\overline{a}_6$ | × | × | × | −0.068993 |
| $\overline{a}_5$ | × | × | × | −0.20917 |
| $\overline{a}_4$ | × | × | −0.24362 | −0.046007 |
| $\overline{a}_3$ | × | × | −0.11944 | −0.13145 |
| $\overline{a}_2$ | × | × | −0.28459 | −0.14177 |
| $\overline{a}_1$ | × | −0.5222 | −0.099561 | −0.076204 |
| $\overline{a}_0$ | −0.95481 | −0.4396 | −0.20984 | −0.090977 |
| $\|\mathcal{E}_{\mathcal{N}}\|$ | 1.5608 | 1.3966 | 1.2316 | 1.2012 |

The measured voltage $v_{e\ell}$ and the responses of discrete-time system $\overline{F}_h(z)$ to the measured current $i_{e\ell}$ with orders $n = 1$, $n = 2$, $n = 5$ and $n = 8$ are plotted in Figure 4. Unlike Figure 3, a negative offset has been introduced in the measured voltage $v_{e\ell}$ in Figure 4 so that $v_{e\ell}$ is initialized to zero. In the same way, a negative offset has been introduced in the measured current $i_{e\ell}$ in Figure 4 so that the responses of discrete-time system $\overline{F}_h(z)$ are initialized to zero.

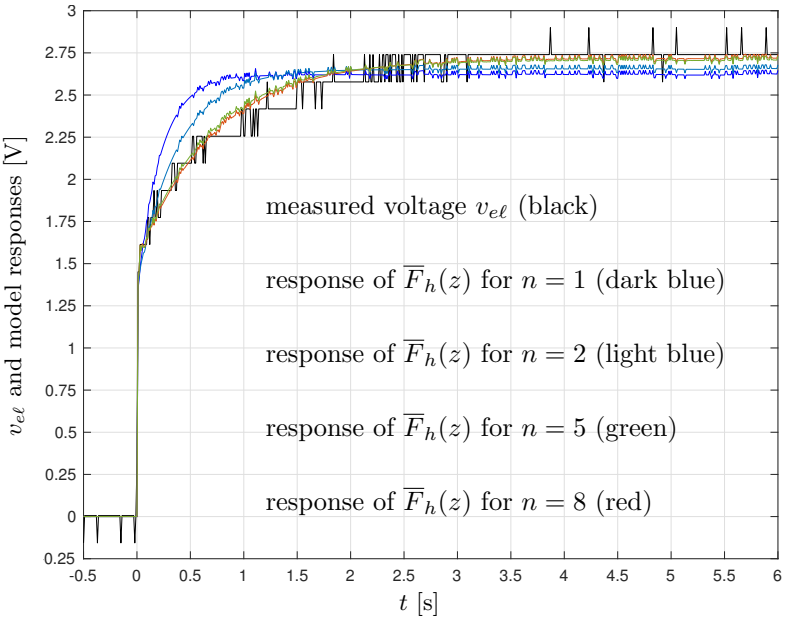


Figure 4: PEM electrolyzer models responses to the measured current $i_{e\ell}$.

It can be seen in Table 2 that $\|\mathcal{E}_{\mathcal{N}}\|$ decreases when the order $n$ increases. This is confirmed in Figure 4, the responses are all the closer to the curve of $v_{e\ell}$ as the order $n$ increases. The steady-state behavior of $v_{e\ell}$ is well captured by all orders although it is improved when the order $n$ increases. The orders $n = 1$ and $n = 2$ fail to correctly reproduce the transient behavior of $v_{e\ell}$. This is not the case for orders $n = 5$ and $n = 8$. However, the improvement obtained with order $n = 8$ compared to $n = 5$ is very small, almost negligible. Therefore, it can be concluded that it is useless to test orders $n > 8$ and the order $n = 8$ is chosen for the sequel of the paper, i.e. the discrete-time transfer function $\overline{F}_h(z)$ defined in (2) is given by (see column where $n = 8$ in Table 2)

$$\overline{F}_h(z) = \frac{\overline{b}_8 z^n + \overline{b}_7 z^7 + \overline{b}_6 z^6 + \overline{b}_5 z^5 + \overline{b}_4 z^4 + \overline{b}_3 z^3 + \overline{b}_2 z^2 + \overline{b}_1 z + \overline{b}_0}{z^8 + \overline{a}_7 z^7 + \overline{a}_6 z^6 + \overline{a}_5 z^5 + \overline{a}_4 z^4 + \overline{a}_3 z^3 + \overline{a}_2 z^2 + \overline{a}_1 z + \overline{a}_0}. \tag{10}$$

2nd step: obtention of a continuous-time model $\widetilde{F}_h(s)$ from $\overline{F}_h(z)$.

A continuous-time transfer function $\widetilde{F}_h(s)$ can be obtained from the discrete-time transfer function $\overline{F}_h(z)$ given in (10) by using the bilinear transform as follows

$$\begin{aligned}
\widetilde{F}_h(s) &= \overline{F}_h(z)\big|_{s=\frac{2}{T_s}\frac{z-1}{z+1}} \\
&= \left.\frac{\begin{pmatrix} 0.056665z^8 - 0.0070842z^7 + 0.00076362z^6 \\ -0.013993z^5 - 0.0021986z^4 - 0.0092568z^3 \\ -0.0078828z^2 - 0.0055324z - 0.0053431 \end{pmatrix}}{\begin{pmatrix} z^8 - 0.17929z^7 - 0.068993z^6 \\ -0.20917z^5 - 0.046007z^4 - 0.13145z^3 \\ -0.14177z^2 - 0.076204z - 0.090977 \end{pmatrix}}\right|_{s=\frac{2}{T_s}\frac{z-1}{z+1}} \\
&= \frac{\begin{pmatrix} 0.062377s^8 + 88.023s^7 + 49583s^6 \\ 2.1988\times10^7 s^5 + 4.6787\times10^9 s^4 + 8.8295\times10^{11} s^3 \\ +6.599\times10^{13} s^2 + 5.2483\times10^{15} s + 1.2587\times10^{16} \end{pmatrix}}{\begin{pmatrix} s^8 + 1568.9s^7 + 8.8721\times10^5 s^6 \\ +3.9591\times10^8 s^5 + 8.3902\times10^{10} s^4 + 1.5336\times10^{13} s^3 \\ +1.1226\times10^{15} s^2 + 8.4538\times10^{16} s + 1.1511\times10^{17} \end{pmatrix}}
\end{aligned} \tag{11}$$

with sample interval $T_s = 0.01$. The transfer function in (11) can be written in state-space form as $\widetilde{F}_h(s) = \widetilde{C}_h(sI_8 - \widetilde{A}_h)^{-1}\widetilde{B}_h + \widetilde{D}_h$ where $\widetilde{D}_h = 0.062377\ \Omega$.

3rd step: obtention of a reduced-order continuous-time model $F_h(s)$.

The system $\widetilde{F}_h(s)$ given in (11) can be approximated by a transfer function $F_h(s)$ of order $n_r$ less than $n = 8$ by means of a balanced truncation proposed by Moore in [47]. The Hankel singular values of any state-space realization of $\widetilde{F}_h(s)$ given in (11) are

$$h_1 = 0.024217, \quad h_2 = 0.0055604, \quad h_3 = 0.0054879, \quad h_4 = 0.0012106,$$
$$h_5 = 0.00070002, \quad h_6 = 0.00050868, \quad h_7 = 0.00042657, \quad h_8 = 0.00020877.$$

For the balanced state-space realization of $\widetilde{F}_h(s)$, these Hankel singular values measure the "influence" of the input $i_{e\ell}$ on the states and of the states on the output $v_{e\ell}$. So an approximated state-space realization of order $n_r < n$ for the system $\widetilde{F}_h(s)$ is obtained by deleting the last $n - n_r$ last states of the balanced state-space realization of $\widetilde{F}_h(s)$, and the error made can be evaluated by the corresponding deleted Hankel singular values [47].

The Hankel singular values of $\widetilde{F}_h(s)$ can be divided into the following three sets: $\mathcal{S}_1 = \{h_1\}$, $\mathcal{S}_2 = \{h_2, h_3\}$ and $\mathcal{S}_3 = \{h_4, h_5, h_6, h_7, h_8\}$. The Hankel singular values in $\mathcal{S}_3$ are very small compared to those in $\mathcal{S}_2$. We can therefore hope to obtain a reduced order model at least equal to 3. The Hankel singular values in $\mathcal{S}_2$ are close. it is therefore necessary to test the reduced orders $n_r = 2$ and $n_r = 3$. The Hankel singular in $\mathcal{S}_2$ are large compared to that in $\mathcal{S}_1$. It is therefore interesting to test the reduced order $n_r = 1$.

For the reduced order $n_r = 1, 2, 3$, we obtain the following approximations for $F_h(s)$

$$\begin{aligned} F_{h_1}(s) &= \frac{0.062377s + 0.13769}{s + 1.2426} \\ &= F_{h_{1a}}(s) + \widetilde{D}_h = \frac{0.060183}{s + 1.2426} + 0.062377, \end{aligned} \tag{12a}$$

$$\begin{aligned} F_{h_2}(s) &= \frac{0.06238s^2 + 0.138s + 0.0002637}{s^2 + 1.247s + 0.002163} \\ &= F_{h_{2a}}(s) + \widetilde{D}_h = \frac{0.060212}{s + 1.2453} + \frac{1.9457{\times}10^{-5}}{s + 0.001737} + 0.062377, \end{aligned} \tag{12b}$$

$$\begin{aligned} F_{h_3}(s) &= \frac{0.06238s^3 + 45.07s^2 + 5900s + 1.225{\times}10^4}{s^3 + 875.38s^2 + 92736s + 1.1043{\times}10^5} \\ &= F_{h_{3a}}(s) + \widetilde{D}_h = \frac{-11.567}{s + 752.31} + \frac{1.9758}{s + 121.87} + \frac{0.057506}{s + 1.2045} + 0.062377. \end{aligned} \tag{12c}$$

In Figure 5, the following curves are plotted: the measured voltage $v_{e\ell}$, the response of discrete-time system $\overline{F}_h(z)$ to the measured current $i_{e\ell}$ with order $n = 8$, and the responses of continuous-time system $F_{h_1}(s)$, $F_{h_2}(s)$ and $F_{h_3}(s)$ to a step of amplitude 24.883 A, where 24.883 is the magnitude of the step current $\imath_{e\ell}$ in Figure 3. Unlike Figure 3, a negative offset has been introduced in the measured voltage $v_{e\ell}$ in Figure 4 so that $v_{e\ell}$ is initialized to zero. In the same way, a negative offset has been introduced in the measured current $i_{e\ell}$ in Figure 5 so that the response of discrete-time system $\overline{F}_h(z)$ is initialized to zero.

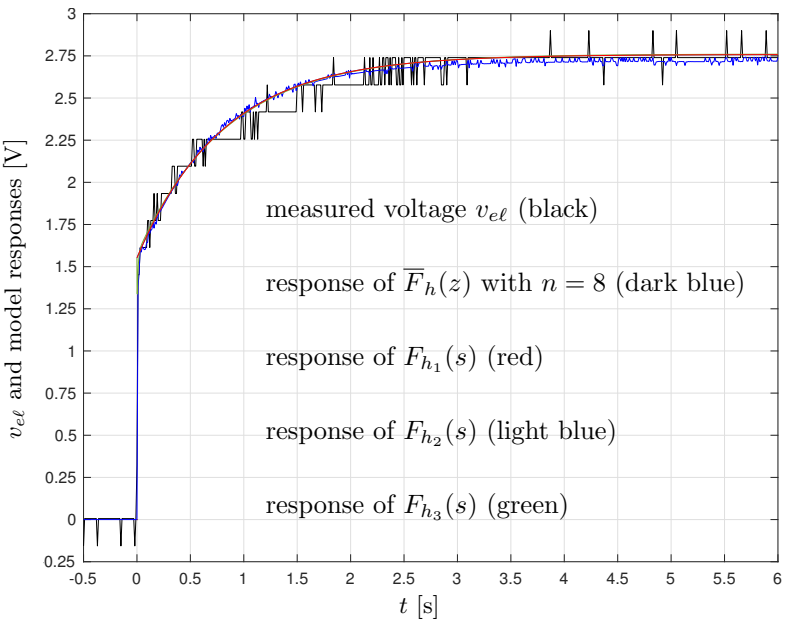


Figure 5: Step responses of PEM electrolyzer and developed models.

In Figure 5, the step responses of $F_{h_1}(s)$, $F_{h_2}(s)$ and $F_{h_3}(s)$ are almost identical and match well with the measured $v_{e\ell}$ and the response of $\overline{F}_h(z)$. This observation is confirmed by the values of the transfer functions in (12):

- we have $F_{h_{1a}}(s) \approx F_{h_{2a}}(s)$ because of the value $1.9457\times10^{-5}$ in the second term in $F_{h_{2a}}(s)$,
- the main time constants in $F_{h_{1a}}(s)$, $F_{h_{2a}}(s)$ and $F_{h_{3a}}(s)$ are close: $T_1 = \dfrac{1}{1.2426} = 0.80479$ s, $T_{2_1} = \dfrac{1}{1.2426} = 0.80304$ s and $T_{3_1} = \dfrac{1}{1.2045} = 0.83023$ s (the difference between $T_1$ and $T_{2_1}$ is due to the rounding in the writing of the number 1.2426 in (12a) and (12b)),
- the time contants $T_{3_2} = \dfrac{1}{121.87} = 0.0082055$ s and $T_{3_3} = \dfrac{1}{752.31} = 0.0013292$ s are much faster than $T_{3_1}$. Their effect can therefore be overlooked in the step response of $F_{h_3}(s)$.

With the analysis made above, the transfer function of 1st order, $F_{h_1}(s)$ given in (12a) is retained as a model for the PEMEL, and we set $F_h(s) = F_{h_1}(s)$ in the sequel of the paper.

Therefore, the 1st order model of the PEMEL with the current $i_{e\ell}$ as input and the voltage $v_{e\ell}$ as output can be described by the $RC$ circuit given in Figure 6,

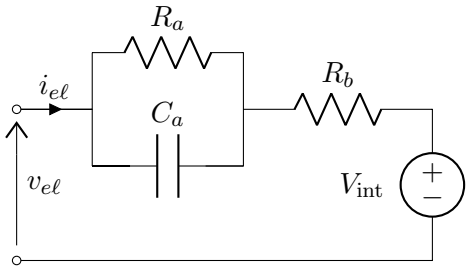


Figure 6: Model of the PEM electrolyzer.

and corresponds to the following state-space model

$$\dot{x}_h = -R_a C_a x_h + R_a i_{e\ell} \tag{13a}$$
$$v_{e\ell} = x_h + R_b i_{e\ell} \tag{13b}$$

which leads to the transfer function $F_h(s)$ given by (see (12a))

$$F_h(s) = \frac{V_{e\ell}(s)}{I_{e\ell}(s)} = \frac{R_a}{R_a C_a s + 1} + R_b$$

$$= \frac{R_a R_b C_a s + R_a + R_b}{R_a C_a s + 1} = \frac{R_b s + \dfrac{R_a + R_b}{R_a C_a}}{s + \dfrac{1}{R_a C_a}}$$
$$= \frac{0.0502s + 0.11081}{0.80479s + 1} = \frac{0.062377s + 0.13769}{s + 1.2426}, \tag{14}$$

with $R_a = 0.048434\ \Omega$, $R_b = 0.062377\ \Omega$ and $C_a = 16.616$ F. The steady-state gain is $k_h = F_h(0) = 0.11081\ \Omega$.

### 2.3 Discussion on the obtained PEM electrolyzer model

The resistors $R_a$ and $R_b$, and the capacitor $C_a$ in model (14) do not have a "physical sense", but allow to better apprehend the complexity of the slow dynamics of the PEMEL. So, equation (14) can be seen as a black-box model. Indeed, to control the PEMEL, a "complete physical model" is not needed: it is enough to have a model that captures both dynamic and static behaviors like model (13).

In the literature, few works have been reported on the dynamic modeling of PEMEL. In [44, 45], the authors have proposed an equivalent electrical circuit to model the dynamics of the PEMEL. However, this modeling is based on previous works focused on modeling of PEM fuel cells without any validation on the real dynamic behavior of PEMEL.

Recently, a first investigation in [35] has been carried out on the analysis of the real dynamics of PEMEL. By studying these dynamics, the authors in [35] have shown that the behavior of PEMEL can be modeled as an equivalent electrical circuit composed by the following part:

- an electromotive force modeling the reversible voltage,
- a resistor modeling the ohmic overvoltage and membrane losses,
- a $RC$ branch modeling the dynamics at the anode, the Gibbs energy, and losses,
- a $RC$ branch modeling the dynamics at the cathode and losses.

It has been emphasized in [35] that the reaction kinetics at the anode is much slower than the reaction kinetics at the cathode. For this reason, the activation phenomena in PEMEL are mainly dominated by the anode reaction. Therefore, this analysis is in agreement with the model in (14) which exhibits a dominant time constant in the behavior of the PEMEL.

Nevertheless, notice that the steady-state behavior has not been studied in [35].

Compared to the previous works reported in the literature (see Section 1), this work aims at designing and comparing two controllers based either on the PEMEL current or voltage. These two variables are strongly linked to the energy efficiency and hydrogen flow rate of the PEMEL. Indeed, the higher the current, the higher the hydrogen flow rate; whereas the higher the stack voltage, the lower the energy efficiency. These controllers are developed to keep up the current or voltage as its reference value whatever the input voltage variations. The reference allows guaranteeing the required energy efficiency or hydrogen flow rate. Besides, the dynamic response of the PEMEL must be taken into consideration while designing the controller to avoid hazardous overshoot; which could damage the PEMEL.

## 3 Stacked interleaved DC-DC buck converter modeling

### 3.1 Presentation of the system

After presenting the developed PEMEL model and the method to determine its parameters, this section is mainly focused on the modeling of the DC-DC converter connected to the PEMEL. In this work, it has been decided to choose a SIBC as the interface between the DC grid and the PEMEL as shown in Figure 7.

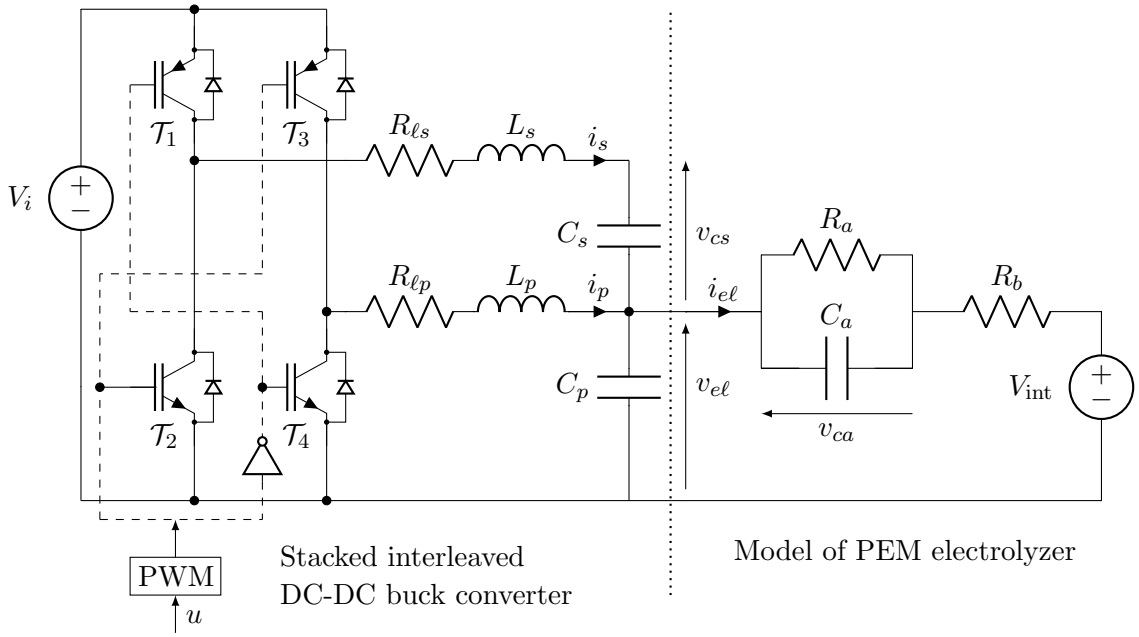


Figure 7: Stacked interleaved DC-DC buck converter with pulse width modulation (PWM) and model of PEM electrolyzer.

Indeed, for PEMEL applications, step-down voltage conversion is requested due to the high input DC voltage and low output DC voltage. The SIBC as shown in Figure 7 is perfectly suitable to meet this issue. Furthermore, SIBC is based on an interleaved structure by paralleling two basic buck converters increasing its availability in case of power switch failures. Compared to a classic interleaved buck converter, the SIBC includes an additional capacitor (i.e. $C_s$) located between the second (i.e. $s$) and first (i.e. $p$) phases. This additional capacitor allows stopping the DC part of the current $i_s$ . Thus, only the AC part of the current $i_s$ flows through the second phase. Besides, since a couple of switches (i.e. $\mathcal{T}_1$ and $\mathcal{T}_4$, $\mathcal{T}_2$ and $\mathcal{T}_3$) is controlled in an opposite way (see Figures 7 and 8), the output current ripple (i.e. $i_{e\ell}$) can be canceled whatever the duty cycle value. To summarize, the couple of switches (i.e. $\mathcal{T}_2$ and $\mathcal{T}_3$) is controlled with a duty cycle equal to $(1 - D)$, whereas the couple (i.e. $\mathcal{T}_1$ and $\mathcal{T}_4$) is controlled with a duty cycle given by $D$, as shown in Figure 8, where $T_c$ is the switching period of the SIBC. Based on Figure 8, during the time period $T_c(1 - D)$, the power switches $\mathcal{T}_2$ and $\mathcal{T}_3$ are closed (ON state); while $\mathcal{T}_1$ and $\mathcal{T}_4$ are open (OFF state). In comparison, during the time period $T_cD$, the power switches $\mathcal{T}_2$ and $\mathcal{T}_3$ are open (OFF state); while $\mathcal{T}_1$ and $\mathcal{T}_4$ are closed (ON state).

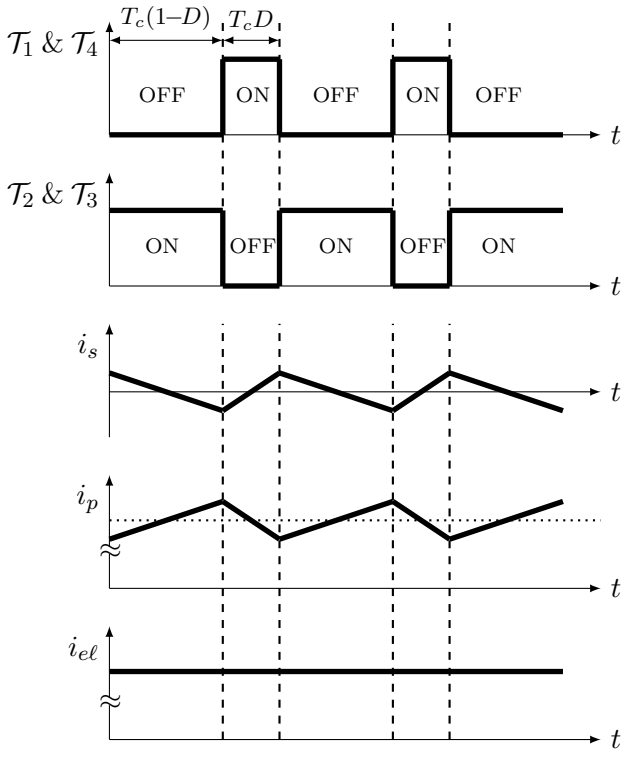


Figure 8: Switching diagram and current waveforms.

The following subsections introduce the state-space averaging modeling and the transfer function of the system.

### 3.2 State-space averaging modeling and transfer function

Based on Figures 7 and 8, the system (including the SIBC and developed PEMEL model) has been modeled by using the state-space averaging techniques to obtain the state-space model [36, 37]. The modeling of the system in this section is different compared to the previous work developed with the SIBC [48] since the proposed dynamic model of the PEMEL is taken into account. Therefore, there is an additional state variable in the system. Thus, a new transfer function is obtained both to regulate the PEMEL current or the voltage.

Based on the control theory for state-space averaging modeling [36, 37], the system is divided into two subsystems: one fit during $DT_c$, another one fit during $(1-D)T_c$. The analysis of these two subsystems enables obtaining two sets of matrix $A$, $B$, and $C$ (i.e. $A_1$, $A_2$, $B_1$, $B_2$, $C_1$, $C_2$). Then, the state-space model can be obtained by averaging the two sets of matrix $A$, $B$, and $C$.

The proposed state-space models during either $DT_c$ (with index $i = 1$), or during $(1-D)T_c$ (with index $i = 2$) are given by

$$\dot{x} = A_i x + B_i u \tag{15a}$$

$$y = C_i x \tag{15b}$$

where $x^T = \begin{bmatrix} i_p & i_s & v_{e\ell} & v_{cs} & v_{ca} \end{bmatrix}$ is the state vector, the voltage $u \in \mathbb{R}$ is the control input and $y^T = \begin{bmatrix} i_{e\ell} & v_{e\ell} \end{bmatrix}$ are the measured outputs.

Applying Kirchhoff's circuit laws in Figure 7 gives

$$A_1 = A_2 = \begin{bmatrix} \frac{-R_{\ell p}}{L_p} & 0 & \frac{-1}{L_p} & 0 & 0 \\ 0 & \frac{-R_{\ell s}}{L_s} & \frac{-1}{L_s} & \frac{-1}{L_s} & 0 \\ \frac{1}{C_p} & \frac{1}{C_p} & \frac{-1}{R_b C_p} & 0 & \frac{1}{R_b C_p} \\ 0 & \frac{1}{C_s} & 0 & 0 & 0 \\ 0 & 0 & \frac{1}{C_a R_b} & 0 & \frac{-(R_a+R_b)}{C_a R_a R_b} \end{bmatrix}, \tag{16a}$$

$$B_1 = \begin{bmatrix} \frac{1}{L_p} \\ 0 \\ 0 \\ 0 \\ 0 \end{bmatrix}, B_2 = \begin{bmatrix} 0 \\ \frac{1}{L_s} \\ 0 \\ 0 \\ 0 \end{bmatrix}, C_1 = C_2 = \begin{bmatrix} 0 & 0 & \frac{1}{R_b} & 0 & \frac{-1}{R_b} \\ 0 & 0 & 1 & 0 & 0 \end{bmatrix}, \tag{16b}$$

and the average state-space model is given by

$$\dot{x} = Ax + Bu \tag{17a}$$

$$y = Cx \tag{17b}$$

where $A = A_1 = A_2$, $B = (B_1 - B_2)V_i$ and $C = C_1 = C_2$.

This model can be simplified since we have $R_\ell = R_{\ell p} = R_{\ell s}$ and $L = L_p = L_s$ in Figure 7, and we obtain

$$A = \begin{bmatrix} \frac{-R_\ell}{L} & 0 & \frac{-1}{L} & 0 & 0 \\ 0 & \frac{-R_\ell}{L} & \frac{-1}{L} & \frac{-1}{L} & 0 \\ \frac{1}{C_p} & \frac{1}{C_p} & \frac{-1}{R_b C_p} & 0 & \frac{1}{R_b C_p} \\ 0 & \frac{1}{C_s} & 0 & 0 & 0 \\ 0 & 0 & \frac{1}{C_a R_b} & 0 & \frac{-(R_a+R_b)}{C_a R_a R_b} \end{bmatrix}, \tag{18a}$$

$$B = \begin{bmatrix} \frac{V_i}{L} \\ \frac{-V_i}{L} \\ 0 \\ 0 \\ 0 \end{bmatrix}, C = \begin{bmatrix} 0 & 0 & \frac{1}{R_b} & 0 & \frac{-1}{R_b} \\ 0 & 0 & 1 & 0 & 0 \end{bmatrix}. \tag{18b}$$

The transfer matrix associated to the state-space model (17)-(18) is given by

$$G(s) = \begin{bmatrix} G_i(s) \\ G_v(s) \end{bmatrix} = \frac{\begin{bmatrix} \frac{V_i(C_a R_a s + 1)}{C_a C_p C_s L^2 R_a R_b} \\ \frac{V_i(C_a R_a R_b s + R_a + R_b)}{C_a C_p C_s L^2 R_a R_b} \end{bmatrix}}{s^5 + c_4 s^4 + c_3 s^3 + c_2 s^2 + c_1 s + c_0}, \tag{19}$$

where $G_i(s)$ and $G_v(s)$ are the transfer functions from $u$ to $i_{e\ell}$ and $v_{e\ell}$, respectively, and

$$c_4 = \frac{C_a C_s L^2 R_a + C_p C_s L^2 R_a + C_p C_s L^2 R_b + 2 C_a C_p C_s L R_a R_b R_\ell}{C_a C_p C_s L^2 R_a R_b}, \tag{20a}$$

$$c_3 = \frac{C_sL^2 + C_aC_pLR_aR_b + 2C_aC_sLR_aR_b + 2C_aC_sLR_aR_\ell}{C_aC_pC_sL^2R_aR_b} + \frac{2C_pC_sLR_aR_\ell + 2C_pC_sLR_bR_\ell + C_aC_pC_sR_aR_bR_\ell^2}{C_aC_pC_sL^2R_aR_b}, \tag{20b}$$

$$c_2 = \frac{C_aLR_a + C_pLR_a + C_pLR_b + 2C_sLR_a + 2C_sLR_b + 2C_sLR_\ell + C_aC_sR_aR_\ell^2}{C_aC_pC_sL^2R_aR_b} + \frac{C_pC_sR_aR_\ell^2 + C_pC_sR_bR_\ell^2 + C_aC_pR_aR_bR_\ell + 2C_aC_sR_aR_bR_\ell}{C_aC_pC_sL^2R_aR_b}, \tag{20c}$$

$$c_1 = \frac{L + C_sR_\ell^2 + C_aR_aR_b + C_aR_aR_\ell + C_pR_aR_\ell + C_pR_bR_\ell + 2C_sR_aR_\ell + 2C_sR_bR_\ell}{C_aC_pC_sL^2R_aR_b}, \tag{20d}$$

$$c_0 = \frac{R_a + R_b + R_\ell}{C_aC_pC_sL^2R_aR_b}. \tag{20e}$$

Notice that relation (19) gives $F_h(s) = \dfrac{G_v(s)}{G_i(s)}$, where $F_h(s)$ is the transfer function in (14).

### 3.3 Numerical values of the model

The numerical values of the electrical components in Figure 7 are given in Table 3.

Table 3: Numerical values of the electrical components in Figure 7.

| **Electrical components** | **Values** | **Units** |
|---|---|---|
| $V_i$ | 30 | V |
| $L = L_p = L_s$ | $426\times10^{-6}$ | H |
| $R_\ell = R_{\ell p} = R_{\ell s}$ | 0.06 | Ω |
| $C_p$ | 0.0001 | F |
| $C_s$ | $10\times10^{-6}$ | F |
| $R_a$ | 0.048434 | Ω |
| $R_b$ | 0.062377 | Ω |
| $C_a$ | 16.616 | F |

Using Table 3 and the matrices given in (18), the transfer matrix $G(s)$ in (19) has the following state-space realization

$$G(s) = \begin{bmatrix} G_i(s) \\ G_v(s) \end{bmatrix} = \left[\begin{array}{c|c} A & B \\ \hline C & 0 \end{array}\right]$$

$$= \left[\begin{array}{ccccc|c} -140.85 & 0 & -2347.4 & 0 & 0 & 70423 \\ 0 & -140.85 & -2347.4 & -2347.4 & 0 & -70423 \\ 10^4 & 10^4 & -1.6032\times10^5 & 0 & 1.6032\times10^5 & 0 \\ 0 & 10^5 & 0 & 0 & 0 & 0 \\ 0 & 0 & 0.9648 & 0 & -2.2073 & 0 \\ \hline 0 & 0 & 16.032 & 0 & -16.032 & 0 \\ 0 & 0 & 1 & 0 & 0 & 0 \end{array}\right]. \tag{21}$$

The poles ($p_i$, $i = 1, \ldots, 5$, for $G_i(s)$ and $G_v(s)$), the zeros ($z_i$ for $G_i(s)$ and $z_v$ $G_v(s)$) and the steady-state gains ($k_i = G_i(0)$ and $k_v = G_v(0)$) are

$$p_1 = -143.22 + 15327j, \qquad p_2 = -143.22 - 15327j,$$
$$p_3 = -1.7373, \qquad p_4 = -287.06,$$
$$p_5 = -1.6002\,10^5$$
$$z_i = \frac{-1}{R_aC_a} = -1.2425, \qquad z_v = \frac{-(R_a + R_b)}{R_aR_bC_a} = -2.2073,$$

$$k_i = G_i(0) = \frac{V_i}{R_a + R_b + R_\ell} = 175.63\ \text{A}, \qquad k_v = G_v(0) = \frac{V_i(R_a + R_b)}{R_a + R_b + R_\ell} = 19.462\ \text{V},$$

where $j$ is the imaginary number satisfying $j^2 = -1$.

We obtain $\dfrac{k_v}{k_i} = k_h = 0.11081\ \Omega$ (see (14)).

The damping factor $\zeta$ and the natural frequency $\omega_n$ associated to the complex poles $p_1$ and $p_2$ are $\zeta = 0.0093439$ and $\omega_n = 15328$ rad/s, where $(s - p_1)(s - p_2) = s^2 + 2\zeta\omega_n + \omega_n^2$.

The real eigenvalues give the three following time constants: $T_1 = \dfrac{-1}{p_3} = 0.5756$ s, $T_2 = \dfrac{-1}{p_4} = 0.0034836$ s and $T_3 = \dfrac{-1}{p_5} = 6.2491{\times}10^{-6}$ s. A fourth time constant $T_4 = \dfrac{1}{\omega_n} = 6.5242{\times}10^{-5}$ s is associated to the complex poles $p_1$ and $p_2$.

The step responses of $G_i(s)$ and $G_v(s)$ are plotted in Figure 9.

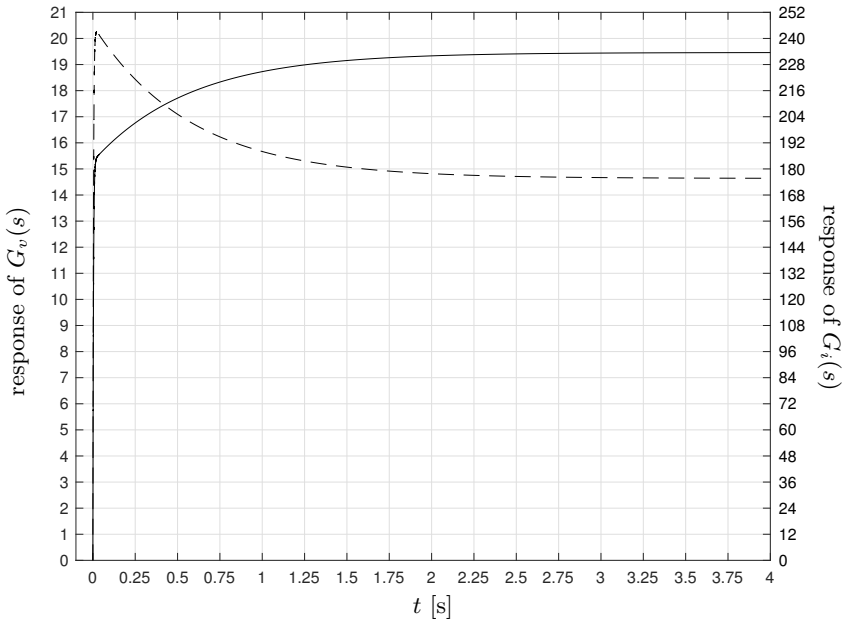


Figure 9: Step responses of $G_i(s)$ (dashed line) and $G_v(s)$ (solid line).

Since $T_1 \gg T_2 \gg T_4 > T_3$, it can be noted that the transient behaviour of the two step responses depends almost exclusively on the time constant $T_1$ with a settling time given by $t_s \approx 3T_1 = 1.7268$ s. The interleaved buck converter has influenced the dynamics of the step responses since the time constant of the model of the PEMEL in Figure 6 is $R_aC_a = 0.80479$ s (see (14)) and is higher than $T_1$.

# 4 PID control

## 4.1 Generalities on PID control

In this section, the model given in (19) is used to synthesize two PID controllers dedicated for the control of the current $i_{e\ell}$ and the voltage $v_{e\ell}$, respectively. In Section 5, these two PIDs are implemented on the experimental test bench including the SIBC and the PEMEL shown in Figure 1 with the features given in Table 1. The control structure is given in Figure 10, where the measurement is either $\overline{y} = v_{e\ell}$ or $\overline{y} = i_{e\ell}$.

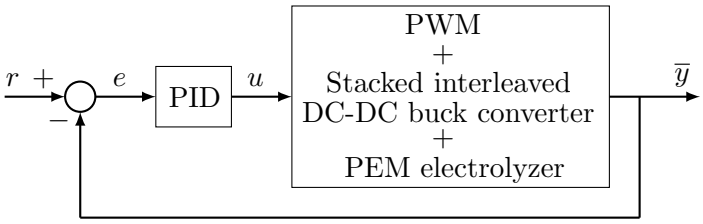

Figure 10: Control structure.

The PID controller in Figure 10 is given by the following transfer function

$$U(s) = K_p \left(1 + \frac{1}{T_i s} + \frac{T_d s}{\tau_d s + 1}\right) E(s) \tag{22}$$

where $K_p$ is the proportional gain, $T_i > 0$ is the integral time constant, $T_d > 0$ is the derivative time constant, and $\tau_d = \dfrac{T_d}{N}$ is the filter time constant with $N = 10$. This type of corrector is used in this work because PIDs are the most used correctors in industrial applications. For a survey on PID control, the reader can see [49, 50, 51, 52].

The following table summarizes the effects of PID parameters $K_p$, $T_i$ and $T_d$ settings on closed loop system behavior.

Table 4: Effects of PID parameters on the step response.

| actions | rise time | settling time | overshoot | steady-state error | stability margin |
|---|---|---|---|---|---|
| $K_p \nearrow$ | $\searrow$ | $\nearrow$ | $\nearrow$ | $\searrow$ | $\searrow$ |
| $\dfrac{K_p}{T_i} \nearrow$ | $\searrow$ | $\nearrow$ | $\nearrow$ | vanish | $\searrow$ |
| $K_p T_d \nearrow$ | $\nearrow$ | $\searrow$ | $\searrow$ | no effect | $\nearrow$ |

As can be seen in Table 4, a PID controller is well adapted to control a PEMEL. For example, the proportional gain $K_p$ can decrease overshoot on the step response due to abrupt variations when considering a RES as power source. The integral action allows to track the reference in spite of variations of operating conditions due weather changes. Rise and settling times can be adjusted with the proportional gain $K_p$ and the derivative time constant $T_d$ (two parameters $K_p$ and $T_d$ are useful since their effects on rise and settling times are antagonistic). In addition, the robustness of the closed loop behavior to modeling error in the transfer function $F_h(s)$ (see (1) and (14)), i.e. the stability margin, can be improved by adjusting the derivative time constant $T_d$.

The tuning of the PID parameters is made in the following three steps:

**1)** Based on the analysis of the transfer function of whole SIBC-PEMEL, (i.e. $G(s)$ in (21)), two design methods for PID tuning are chosen in Section 4.2.
**2)** The tuning of the PID controllers is made in Section 4.3.
**3)** Some remarks on the obtained stability margins are made in Section 4.4.

## 4.2 Model analysis for the choice of the PID controllers synthesis methods

As can be seen classical works on PID design [53, 54, 55] and in textbooks and report on PID control [49, 50, 51, 52], many tuning approaches for PID parameters are based on the step response of the open loop process to be controlled. This step response, also called process reaction curve in the literature, should exhibit a horizontal tangent at the origin, this horizontal tangent at the origin being approximated by a pure time delay in the literature. In addition, this step response should be monotonic with a positive slope. The steps responses of $G_i(s)$ and $G_v(s)$ do not exhibit a horizontal tangent at the origin or a pure time delay as shown in Figure 9. In addition, the step response of $G_i(s)$ in Figure 9 presents a decreasing behavior. Therefore, the PID tuning based on open loop step response models described in the literature can not be used.

In the sequel, two tuning approaches are retained in this work to determine the coefficients of the PID controllers for the PEMEL:

- a step by step method initially presented by Prouvost in [56] and modified in [57],
- the phase margin method proposed by Åström and Hägglund [58].

Before applying the two above-mentioned methods, a frequency analysis of systems $G_i(s)$ and $G_v(s)$ is made to help the tuning of the PID controllers. The Bode diagrams of $G_i(s)$ and $G_v(s)$ are plotted in Figures 11 and 12.

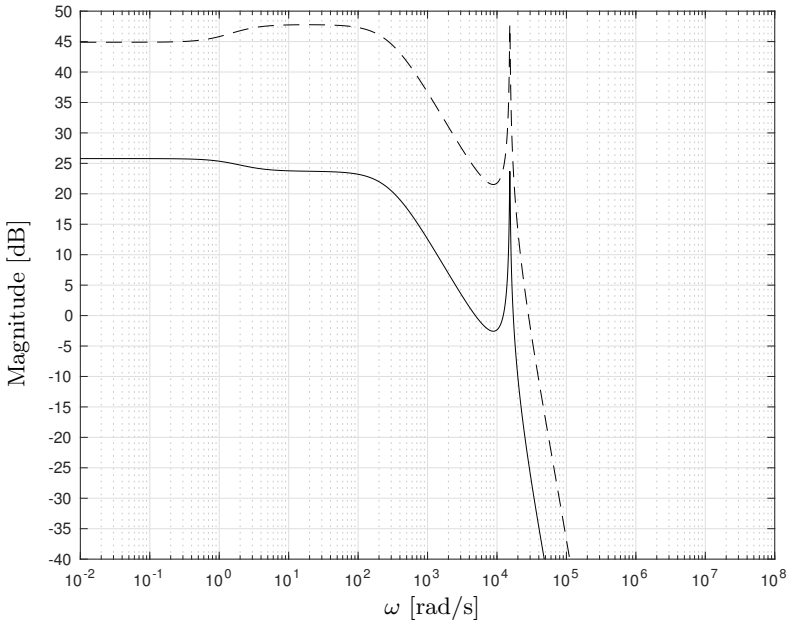


Figure 11: Magnitudes of $G_i(s)$ (dashed line) and $G_v(s)$ (solid line).

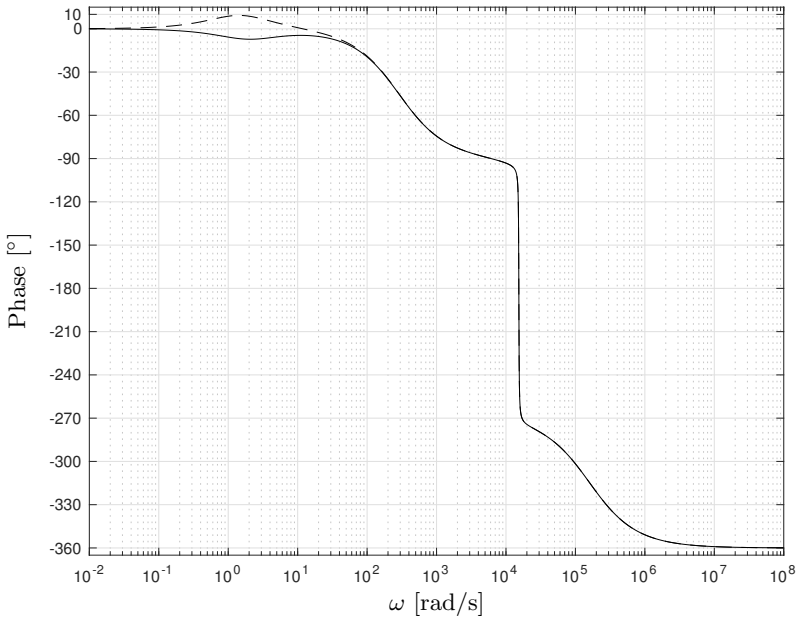


Figure 12: Phases of $G_i(s)$ (dashed line) and $G_v(s)$ (solid line).

As can be seen in Figures 11 and 12, the frequency range $[10^4 \;\; 2\times10^4]$ rad/s is very important:

**i)** Due to a very small damping factor ($\zeta = 0.0093439$), the magnitudes of $G_i(s)$ and $G_v(s)$ have a huge peak at $\omega_p = 15325$ rad/s (see Figure 11): $|G_i(j\omega_p)| = 244.9816$ (i.e. 47.78267 dB) and

$|G_v(j\omega_p)| = 15.2812$ (i.e. 23.6831 dB). A bad adjustment of the PID parameters around this frequency can generate oscillations in the step response in closed loop.
Notice that the derivative action gives high gain in high frequencies. Then, the derivative time constant $T_d$ should be chosen such that $\frac{1}{T_d} > \omega_p$ to avoid an oscillatory behavior in closed loop.

**ii)** For $G_i(s)$ and $G_v(s)$, the ultimate frequency $\omega_{\text{osc}} = 15316.55$ rad/sec (i.e. $\arg(G_i(j\omega_{\text{osc}})) = \arg(G_v(j\omega_{\text{osc}})) = -180°$) is close to $\omega_p$. At $\omega_{\text{osc}}$, the phases of $G_i(s)$ and $G_v(s)$ have an inflection point with an almost vertical tangent (see Figure 12). This ultimate frequency is associated to the ultimate period $T_{\text{osc}} = 4.1022\times10^{-4}$ s and the gain margin is computed at this frequency. In the sequel, the gain margins, which are also called critical gains, are denoted $K_{\text{osc}_i}$ for $G_i(s)$ and $K_{\text{osc}_v}$ for $G_v(s)$. In Figure 11, we have $|G_i(j\omega_{\text{osc}})| = 244.57$ (i.e. 47.768 dB) and $|G_v(j\omega_{\text{osc}})| = 15.256$ (i.e. 23.669 dB). So, the gain margins for $G_i(s)$ and $G_v(s)$ are $K_{\text{osc}_i} = \frac{1}{|G_i(j\omega_{\text{osc}})|} = 0.0040888$ and $K_{\text{osc}_v} = \frac{1}{|G_v(j\omega_{\text{osc}})|} = 0.06555$.
The above discussion has two consequences for the improvement of the gain margin:

- The proportional gain $K_p$ of the PID controllers should be less than $K_{\text{osc}_i}$ for the current control and $K_{\text{osc}_v}$ for the voltage control.
- Since the derivative action gives high gain in high frequencies, the derivative time constant $T_d$ should be chosen such that $\frac{1}{T_d} > \omega_{\text{osc}}$.

This frequency analysis is important since the problems due to the frequency range $[10^4 \;\; 2\times10^4]$ rad/s do not appear in the step responses in Figure 9. Indeed, this frequency range is associated with the time constant $T_4 = \frac{1}{\omega_n} = 6.5242\times10^{-5}$ s which is very small compared to the time constants $T_1 = \frac{-1}{p_3} = 0.5756$ s and $T_2 = \frac{-1}{p_4} = 0.0034836$ s (see the paragraph below Figure 9).

## 4.3 PID tuning

This section is devoted to the tuning of the PID parameters. For each of the two tuning methods retained in Section 4.2, we proceed as follows. First, the PID design methods are presented in Section 4.3.1, and, second, it will be applied on the transfer functions $G_i(s)$ and $G_v(s)$ leaning on the above frequency analysis in Section 4.3.2.

### 4.3.1 Presentation of the retained PID tunings

#### 4.3.1.1 Step by step method [56, 57]

The step by step method consists of successively adjusting the PID parameters in closed loop. This adjustment is based on the effects of PID parameters on the step response summarized in Table 4.

The adjustment of the PID parameters is carried out in the following order.

**1)** Tuning of the proportional gain $K_p$. Only the proportional part of the PID (22) is considered at this step. With the help of the 1st row of Table 4, a value of $K_p$ can be obtained such that the overshoot is not higher than 25 % with a rise time "sufficiently" low.

**2)** Tuning of the derivative time constant $T_d$. Now, the proportional and derivative parts of the PID (22) are taken into account with $K_p$ obtained in the previous step. Using the 3rd row of Table 4, a value of $T_d$ can be determined such that the rise time and the overshoot are both decreased.

**3)** Tuning of the integral time constant $T_i$. The proportional gain obtained in the first step is increased by 10 %, i.e. $K_p$ is replaced by $1.1K_p$. Initially, the integral time constant $T_i$ is chosen "sufficiently large" to exhibit no overshoot in the closed loop step response despite a settling time which can be "very" high. If it is not the case, the value of $T_i$ should be increased. Then, as it is mentioned in the 2nd row of Table 4, $T_i$ is progressively decreased to obtain a settling time which is satisfactory without overshoot or with low overshoot.

#### 4.3.1.2 Phase margin method of Åström and Hägglund [58]

This method does not require to know the transfer function of the plant to be controlled, but only the critical gain $K_{\text{osc}}$ and the ultimate frequency $\omega_{\text{osc}}$ of this plant. $K_{\text{osc}}$ is the gain margin which corresponds to the ultimate gain obtained by using the Ziegler-Nichols continuous cycling method given in [53] and $\omega_{\text{osc}} = \dfrac{2\pi}{T_{\text{osc}}}$ where $T_{\text{osc}}$ is the ultimate period.

Let $\phi_m$ be the desired phase margin. The PID parameters are given by [58]

$$K_p = K_{\text{osc}} \cos(\phi_m), \tag{23a}$$

$$T_d = \frac{T_{\text{osc}}}{4\pi} \left( \tan(\phi_m) + \sqrt{\frac{4}{\alpha} + \tan^2(\phi_m)} \right), \tag{23b}$$

$$T_i = \alpha T_d, \tag{23c}$$

where $\alpha > 1$. $\alpha$ can be used as a tuning parameter to improve the closed loop response. The constraint $\alpha > 1$ allows having $T_i > T_d$, which leads to a low-frequency range for the integral action and to a high-frequency range for the derivative action, without intersection between these two frequency ranges.

Notice that the obtained phase margin may not exactly match $\phi_m$ since the computation of $\tau_d$ is not included in the method, i.e. the three formula in (23) assume that $\tau_d = 0$ in (22).

### 4.3.2 PID control of the current $i_{e\ell}$ and the voltage $v_{e\ell}$

The application of the two methods described in Section 4.3.1 has given the following results.

- Step by step method [56, 57], Section 4.3.1.1: The closed loops in current and in voltage obtained with the PID controllers have a good behavior with good stability margins. In the sequel, the PID for current and voltage controls are called $C_1(s)$ and $C_2(s)$, respectively

$$C_1(s) = K_p \left( 1 + \frac{1}{T_i s} + \frac{T_d s}{\frac{T_d}{N} s + 1} \right) = 0.001 \left( 1 + \frac{1}{0.00205 s} + \frac{8.333{\times}10^{-5} s}{\frac{8.333{\times}10^{-5}}{10} s + 1} \right), \tag{24}$$

$$C_2(s) = K_p \left( 1 + \frac{1}{T_i s} + \frac{T_d s}{\frac{T_d}{N} s + 1} \right) = 0.004 \left( 1 + \frac{1}{0.00168 s} + \frac{8.375{\times}10^{-5} s}{\frac{8.375{\times}10^{-5}}{10} s + 1} \right). \tag{25}$$

- Phase margin method of Åström and Hägglund [58], Section 4.3.1.2: The closed loops in current and in voltage obtained with the PID controllers are unstable for all desired phase margins $\phi_m \in [5^\circ \;\; 80^\circ]$. Nevertheless, the closed loop in voltage is stable with $\phi_m = 85^\circ$, while the one in current is unstable. For this reason, only one PID was selected with $\phi_m = 85.531^\circ$, which is the phase margin obtained with the PID for voltage control for the step by step method. This PID for voltage control with $\phi_m = 85.531^\circ$ is called $C_3(s)$ in the sequel

$$C_3(s) = K_p \left( 1 + \frac{1}{T_i s} + \frac{T_d s}{\frac{T_d}{N} s + 1} \right) = 0.0051079 \left( 1 + \frac{1}{0.0083581 s} + \frac{0.00083581 s}{\frac{0.00083581}{10} s + 1} \right). \tag{26}$$

To explain the tuning of the PID parameters using the frequency analysis made in Section 4.3.2, the Bode diagrams of the PID controllers, plotted in Figures 13 and 14, and the Bode diagrams of the loop gains, plotted in Figures 15 and 16, are needed.

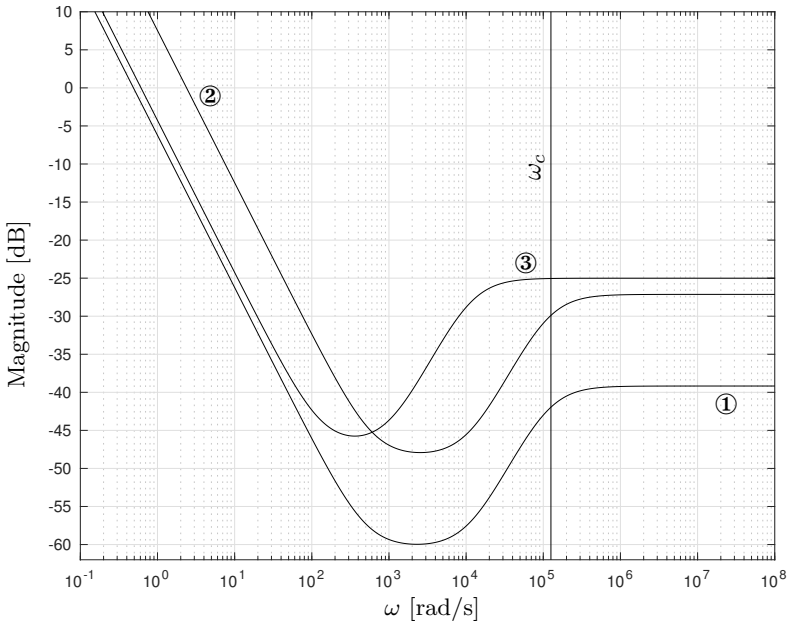


Figure 13: Magnitudes of PID controllers $C_1(s)$ (①), $C_2(s)$ (②) and $C_3(s)$ (③).

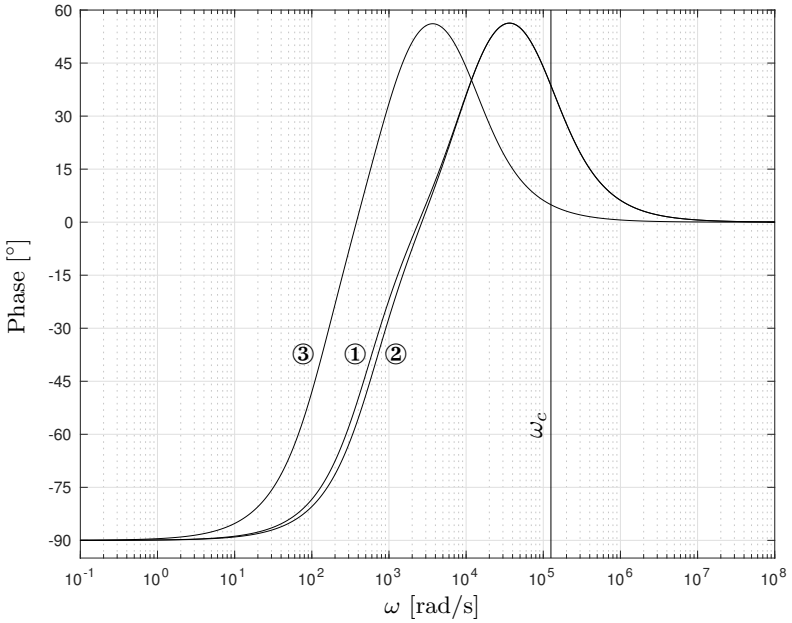


Figure 14: Phases of PID controllers $C_1(s)$ (①), $C_2(s)$ (②) and $C_3(s)$ (③).

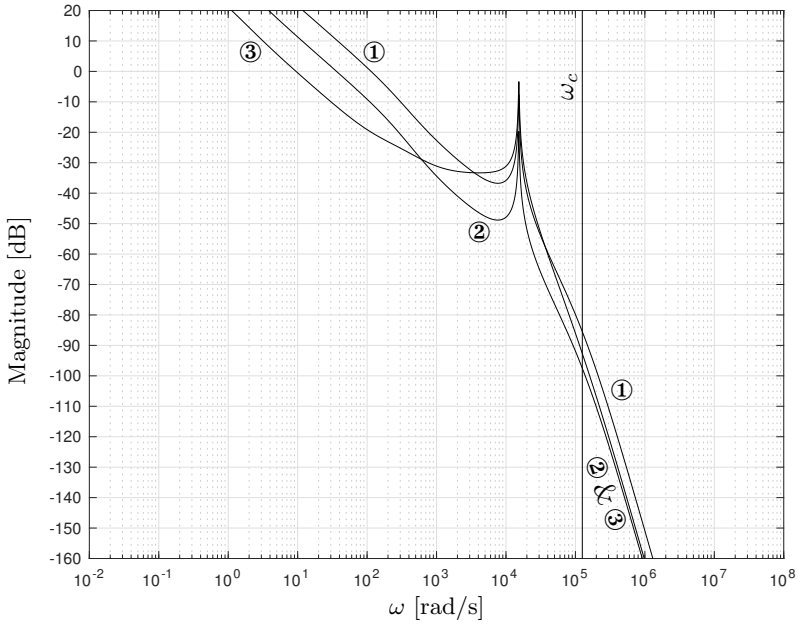


Figure 15: Magnitudes of loop gains $G_i(s)C_1(s)$ (①), $G_v(s)C_2(s)$ (②) and $G_v(s)C_3(s)$ (③).

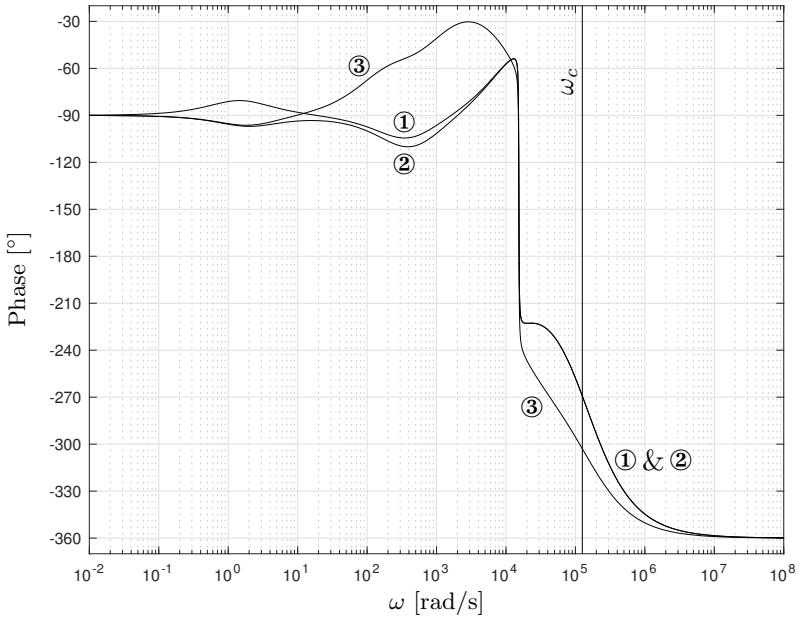


Figure 16: Phases of loop gains $G_i(s)C_1(s)$ (①), $G_v(s)C_2(s)$ (②) and $G_v(s)C_3(s)$ (③).

The switching period of the SIBC is $T_c = 50\,\mu$s, which corresponds to a frequency $\omega_c = 125663.71$ rad/s. The frequency $\omega_c$ must be taken into account in the design of the PID controllers.

#### 4.3.2.1 Application of step by step method

In the sequel, the PID for current and voltage controls are called $C_1(s)$ and $C_2(s)$, respectively.

- Design of PID $C_1(s)$ for system $G_i(s)$. Since $K_{\text{osc}_i}$ is the gain margin, a low value is chosen to initialize the gain $K_p$ for the step by step method (see item (ii) in Section 4.2 for the value of $K_{\text{osc}_i}$).
  Now, the analysis made in item (i) in Section 4.2 is used. So as not to excite the peak in the magnitude plot in Figure 11 in the frequency range $[10^4 \;\; 2\times10^4]$ rad/s, the values of $K_p = \dfrac{0.001}{1.1}$ and $T_d = 8.333\times10^{-5}$ s have been obtained at the 2nd step of the method. Indeed, the more $T_d$ is small, the less the magnitude peak is excited by the 20 dB/dec slope due to derivative action (see

curve ① in Figure 13). The amplitude of this peak has decreased a lot in Figure 15, which allows to increase the closed loop damping factor. In addition, $T_d$ can not be chosen too small because $\omega_c$ must be greater than $\frac{1}{T_d}$.
To complete this analysis (see item (ii) in Section 4.2), notice that small $K_p$ and $T_d$ are required to ensure closed loop stability (see Figures 11 and 12): the magnitude of $G_i(s)C_1(s)$ must be less than 1 when the phase of $G_i(s)C_1(s)$ is equal to $-180°$ (see Figures 15 and 16).
At the 3rd step of the method, with $K_p = 0.001$ and $T_d = 8.333\times10^{-5}$ s, the derivative time constant $T_i$ is adjusted to obtain a sufficiently settling time without overshoot (see the 3rd step in Section 4.3.1).

- Design of PID $C_2(s)$ for system $G_v(s)$. The magnitudes of $G_i(s)$ and $G_v(s)$ are almost parallel, and the phases of $G_i(s)$ and $G_v(s)$ are almost equal except in the frequency interval $0.1 \leqslant \omega \leqslant 10$ rad/s. So, the PID tuning for voltage control is almost similar to the one for current the discussion on the design of PID $C_2(s)$ is similar to that on design of PID $C_1(s)$, but there are fewer constraints for the design of $C_2(s)$ than that of $C_1(s)$. Indeed, curve ② is below the curve ① in Figures 11 and 12, and $K_{\text{osc}_v} > K_{\text{osc}_i}$. This explains the values of $K_p$, $T_i$ and $T_d$ obtained for $C_2(s)$ compared to those of $C_1(s)$ and that is the reason why the discussion on $C_2(s)$ is not detailed.

In Figures 13, 14, 15 and 16, although the derivative time constant $T_d$ is small for PID $C_1(s)$ and $C_2(s)$, and therefore that the frequency $\frac{1}{T_d}$ in rad/s is large, the frequency range for the derivative action is smaller than the SIBC switching frequency $\omega_c$.

#### 4.3.2.2 Application of phase margin method

This PID for voltage control with $\phi_m = 85.531°$ is called $C_3(s)$ in the sequel.

- Design of PID $C_3(s)$ for system $G_v(s)$. According to the above discussion on PID controllers $C_1(s)$ and $C_2(s)$, the parameter $K_p$ and $T_d$ should be sufficiently small. Since $\phi_m = 85.531°$, relation (23a) gives a proportional gain $K_p$ which is almost as small as for $C_2(s)$, however $\tan^2(\phi_m)$ is much larger than $\frac{4}{\alpha}$ in relation (23b) with $\alpha > 1$. Therefore all the values of $\alpha > 2$ lead to values of $T_d$ which are very close to the one obtained for PID $C_3(s)$. As can be seen in Figures 13 and 14, the frequency range in which the derivative action for $C_3(s)$ acts is a decade before that the one for $C_2(s)$. The consequence can be read in figure 15: the peak is larger for $C_3(s)$ than for $C_2(s)$.
In (23b) and (23c), $\alpha = 10$ has been chosen, while $\frac{T_i}{T_d} = 20.06$ for PID $C_2(s)$. It should be noticed that choosing $\alpha = 20.06$ has no influence in the behavior of PID $C_3(s)$ because $T_d = 0.00083555$ s with $\alpha = 20.06$ instead of $T_d = 0.00083581$ s with $\alpha = 10$.

### 4.4 Stability margins

The stability margins obtained with the PID controllers are given in Table 5, where the modulus margin is the minimum distance of the Nyquist plots of $C_1(s)G_i(s)$, $C_2(s)G_v(s)$ or $C_3(s)G_v(s)$ from the critical point $(-1, 0)$ of the complex plane.

Table 5: Stability margins with PID controllers.

| | PID $C_1(s)$ | PID $C_2(s)$ | PID $C_3(s)$ |
|---|---|---|---|
| gain margin | 3.3075 | 13.239 | 1.707 |
| phase margin | 81.719° | 85.531° | 89.911° |
| modulus margin | 0.65361 | 0.91125 | 0.38831 |

Table 5 shows that PID $C_1(s)$ provides good stability margins. PID $C_2(s)$ generates very good stability margins, especially the modulus margin which is close to 1. But it is not the case for PID $C_3(s)$. Indeed, although the phase margin is good with PID $C_3(s)$, the gain and modulus margins are small. In the sequel of this section, the comments on the stability margins given in Table 5 are based on a

frequency analysis with Bode diagrams, while the obtained closed loop time responses are presented in Section 5.

To end this discussion, notice that gain and phase margins given in table 5 can be deduced using Figures 15 and 16.

# 5 Experimental results

## 5.1 Description of the experimental test bench

To evaluate the performances of the different PID controllers (both for PEMEL current and voltage) designed in Section 4, a fit experimental test rig has been realized in the GREEN laboratory at IUT de Longwy as shown in Figure 17. The description of the experimental test rig is provided in the caption of Figure 17. The developed PID control laws have been realized through Matlab/Simulink environment. Afterthat, the control laws have been transfered into a dSPACE DS1104 board to generate the PWM gate control signals to drive the power swithes of the SIBC. Since the PID control laws are based either on PEMEL current or voltage, the measurements are achieved through a current clamp PAC 12 from Chauvin Arnoux Company and a voltage probe MTX 1032-B from Metrix Company. The PWM control signals generated from the dSPACE DS1104 board are 0-5V and therefore, they are not fit to drive the SEMIKRON driver boards SKHI 22 requiring a voltage level 0-15 V. As a result, an interface board has been designed (located between the dSPACE DS1104 board and driver boards) to adapt the input control signals from 0-5 V to output control signals 0-15 V. The system specifications of the PEMEL and SIBC have been provided respectively in Sections 2 and 3. The switching frequency of the SIBC has been selected to 20 kHz to decrease the switching losses, which corresponds to a switching period of the SIBC given by $T_c = 50\,\mu$s.

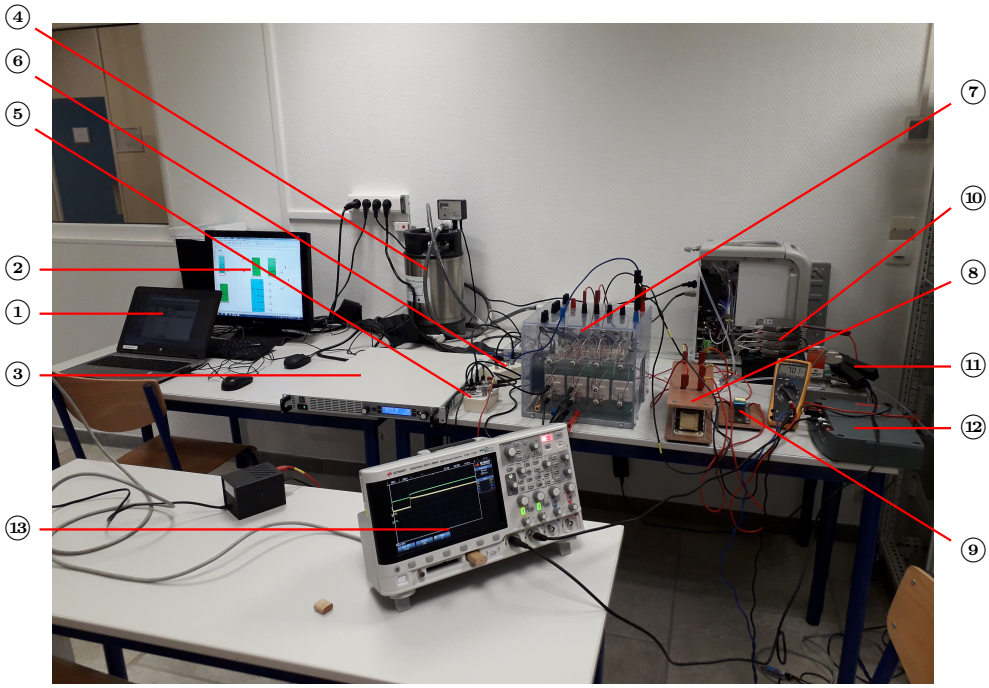


Figure 17: Experimental test rig to validate PID control laws: ① → laptop with a virtual control panel for the DC power supply, ② → computer including Matlab/Simulink and dSPACE ControlDesk softwares, ③ → DC power supply (input), ④ → pure water tank, ⑤ → interface board, ⑥ → dSPACE DS1104 board, ⑦ → IGBT module stack to realize the SIBC, ⑧ → inductive components (i.e. $L_p$, $L_s$), ⑨ → capacitive components (i.e. $C_p$, $C_s$), ⑩ → PEMEL, ⑪ → current clamp, ⑫ → voltage probe, ⑬ → 4-channel digital oscilloscope.

In the next subsection, experimental results are presented and commented to assess the performances of the different designed and tuned PID controllers to control either the current or the voltage.

### 5.2 Experimental results for the PID control laws

The PID current controller $C_1(s)$ and voltage controllers $C_2(s)$ and $C_3(s)$ have been tested experimentally and have given the following responses:

- Figure 18: closed loop step response of the current $i_{e\ell}$ with the PID controller $C_1(s)$ where the measured feedback is $i_{e\ell}$,
- Figure 19: closed loop step response of the voltage $v_{e\ell}$ with the PID controller $C_1(s)$ where the measured feedback is $i_{e\ell}$,
- Figure 20: closed loop step response of the voltage $v_{e\ell}$ with the PID controller $C_2(s)$ where the measured feedback is $v_{e\ell}$,
- Figure 21: closed loop step response of the current $i_{e\ell}$ with the PID controller $C_2(s)$ where the measured feedback is $v_{e\ell}$,
- Figure 22: closed loop step response of the voltage $v_{e\ell}$ with the PID controller $C_3(s)$ where the measured feedback is $v_{e\ell}$,
- Figure 23: closed loop step response of the current $i_{e\ell}$ with the PID controller $C_3(s)$ where the measured feedback is $v_{e\ell}$,

It shall be noticed that the six Figures 18-23 correspond only to three tests: the first for Figures 18-19, the second for Figures 20-21, and the third for Figures 22-23. The current responses are slower than the voltage ones. Therefore, the time axis is 0.038 seconds in Figures 18, 21 and 23, while the time axis is 0.010 seconds in Figures 19, 20 and 22.

A decimation phenomenon affects the six Figures 18-23. This is due to the 4-channel digital oscilloscope used to record the values of the current and the voltage in the experimental test bench (see ⑬ in Figure 17). However, this decimation phenomenon does not act on the closed loop behavior since the record with the 4-channel digital oscilloscope is outside the closed loop.

Based on Figures 18-23, the performances in closed loop of the PID controllers are summarized in Table 6.

Table 6: Closed loop performances of PID controllers.

| | PID $C_1(s)$ | PID $C_2(s)$ | PID $C_3(s)$ |
|---|---|---|---|
| voltage settling time in second | 0.002 | 0.002 | 0.002 |
| current settling time in second | 0.022 | 0.022 | 0.026 |
| $1^{\text{st}}$ overshoot for current in percent | 21.102 | 17.949 | 25 |

From the obtained responses, it can be observed that the three voltage dynamics are similar, without overshoot and faster than the current dynamics. The settling time for the current dynamics is similar for PID $C_1(s)$ and $C_2(s)$, but is a little bit higher for PID $C_3(s)$. The lowest overshoot in the current response is obtained with PID $C_2(s)$ while the highest one is obtained with PID $C_3(s)$.

So, we can conclude that the two PID designed with step by step method ($C_1(s)$ and $C_2(s)$) present better performances than the PID method based on phase margin ($C_3(s)$).

In Figures 18-19, the controlled variable $i_{e\ell}$ converges more slowly than the non-controlled variable $v_{e\ell}$, whereas in Figures 20-21 and 22-23, this is not the case: the controlled variable $v_{e\ell}$ converges more quickly than the non-controlled variable $i_{e\ell}$. In addition, the steady-state behavior in Figure 18 begins at time instant $t = 0.03$ s while it starts at $t = 0.034$ s in Figures 21 and 23. The difference between these two time instants is higher to the voltage settling time (see Table 6). Thus, it is more appropriate to control the current instead of the voltage to get better action on the dynamics of both controlled and non-controlled variables.

In conclusion, based on the previous observations, for small-scale PEM electrolyzer, it makes more sense to control the current instead of the stack voltage, since the desired hydrogen flow rate can be directly obtained by regulating the electrolyzer current. Furthermore, the small-scale studied PEMEL can be seen as a high current-low voltage load: the stack voltage range is very small included between 4.4 V and 8 V, while the current range is quite high, between 0 A and 50 A (see Table 1). Stack voltage regulation is particularly suitable for large-scale alkaline electrolyzers since their voltage range

are extended [46]. For this application, stack voltage regulation is achieved through the use of thyristors-based rectifiers.

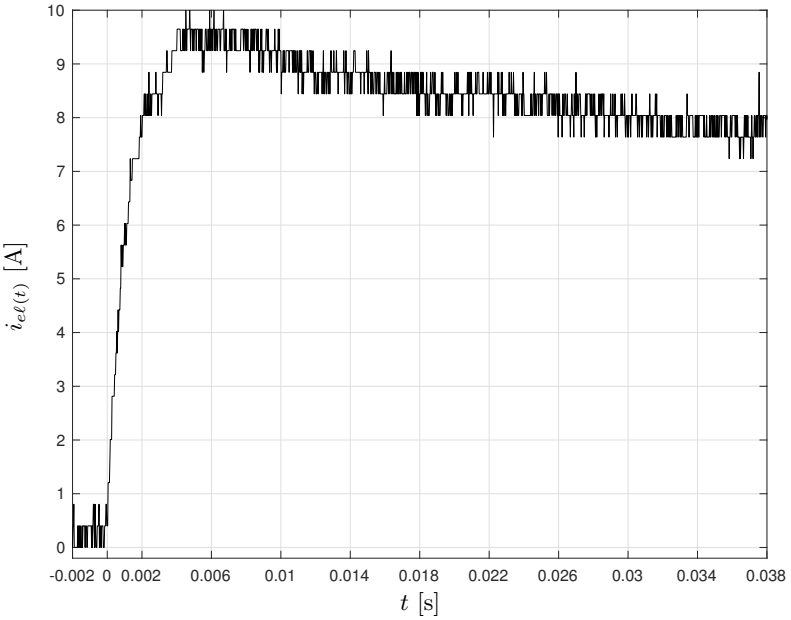


Figure 18: Closed loop step response of the current $i_{e\ell}$ with the current PID $C_1(s)$.

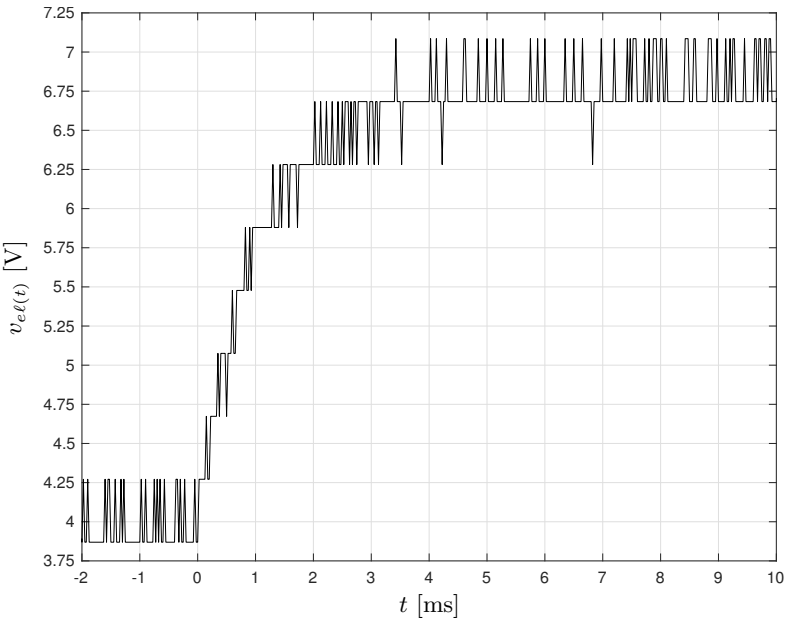


Figure 19: Closed loop step response of the voltage $v_{e\ell}$ with the current PID $C_1(s)$.

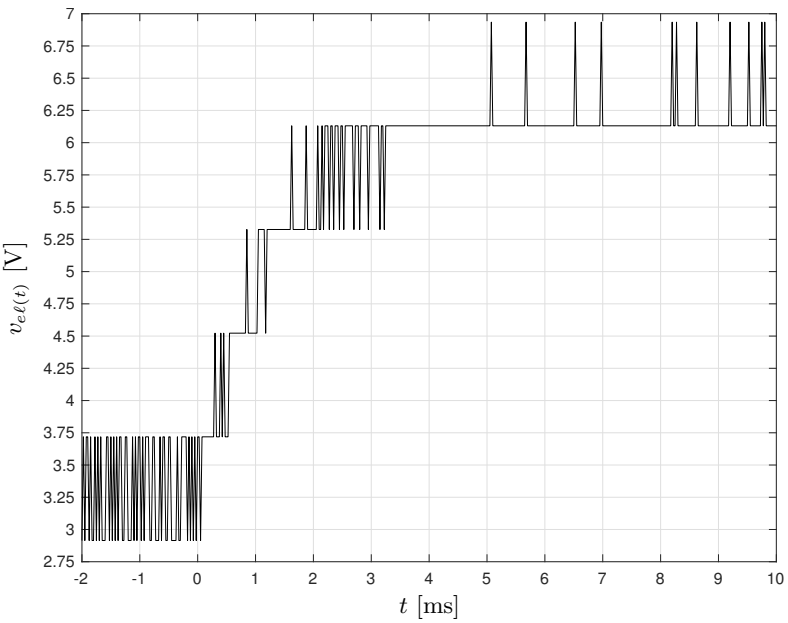

Figure 20: Closed loop step response of the voltage $v_{e\ell}$ with the voltage PID $C_2(s)$.

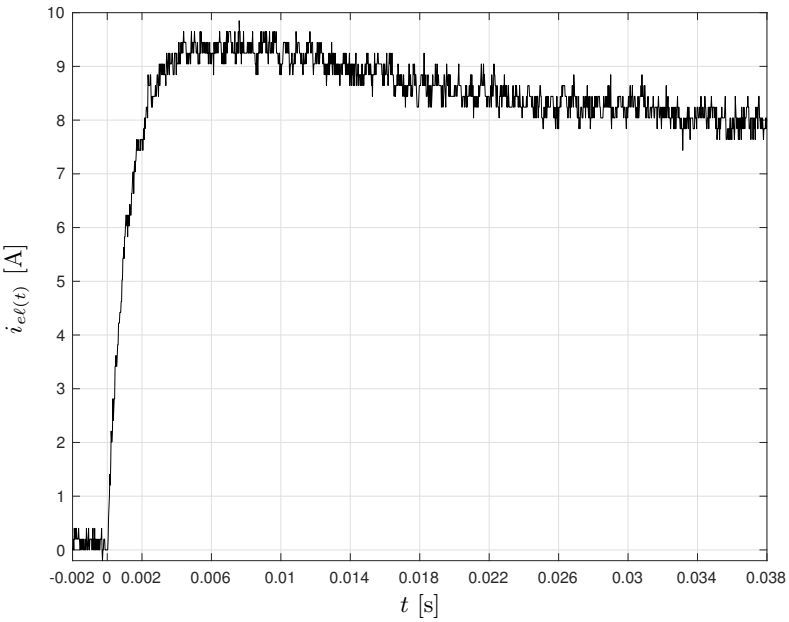

Figure 21: Closed loop step response of the current $i_{e\ell}$ with the voltage PID $C_2(s)$.

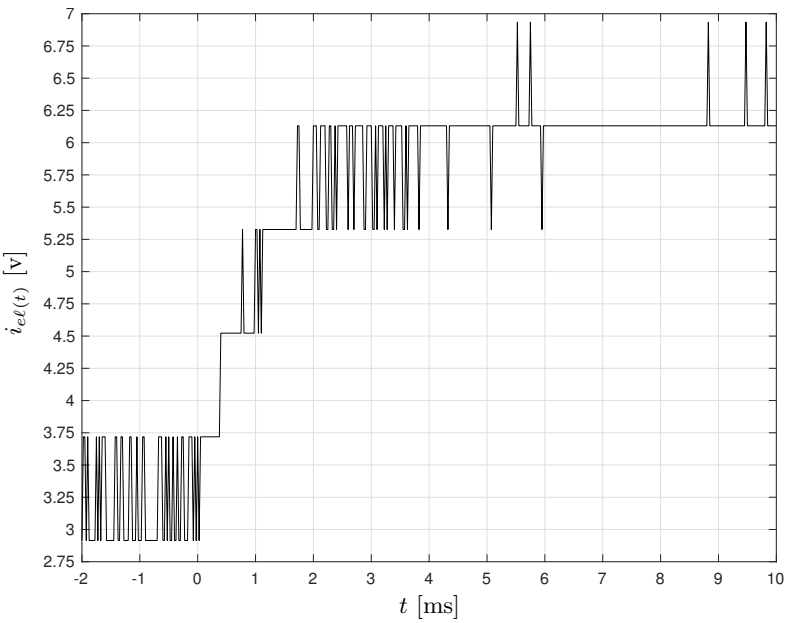


Figure 22: Closed loop step response of the voltage $v_{e\ell}$ with the voltage PID $C_3(s)$.

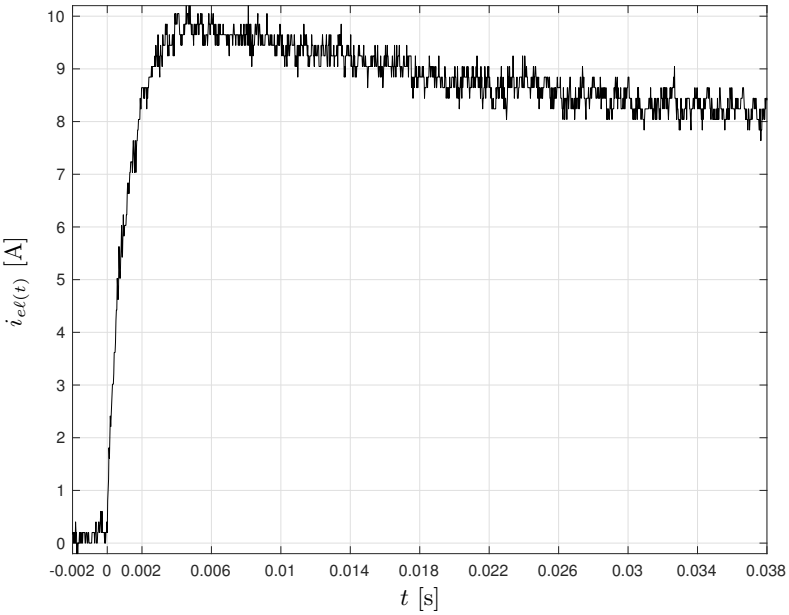


Figure 23: Closed loop step response of the current $i_{e\ell}$ with the voltage PID $C_3(s)$.

# 6 Conclusion

The main purpose of this article was to propose a methodology to design PID controllers based either on voltage or current regulation applied to a stacked interleaved DC-DC buck converter for PEMEL applications.

Unlike the approaches usually developed in the literature where the PEMEL is modeled as a resistive load, the determination of the parameters of the PID controllers takes into account the dynamic behavior of the PEMEL. So, a model of the PEMEL has been first obtained through a least-square algorithm with input-output measured data (current-voltage). Second, the obtained discrete-time model of the PEMEL has been converted into a continuous time one and then combined with the used DC-DC converter state-space description.

Notice that the shape of the step responses of the obtained models does not allow to use standard PID tuning methods based on open loop step response models, which are proposed in the literature. For this reason, an alternative tuning approach based on a step by step method has been retained. For comparison purposes, phase margin method proposed in the literature has also been taken into consideration.

To assess the performances of the developed PID controller tunings, experiments have been carried out on a fit experimental test bench. Based on the obtained results, the step by step method has given better performances than the phase margin method, this latter has not worked in current control configuration. Finally, based on the analysis of the experimental results, it is more suitable to use a current control configuration instead of a voltage control configuration for the investigated small-scale PEM electrolyzer, which can be considered as a high current-low voltage load. Indeed, by controlling the current instead of the stack voltage, the desired hydrogen flow rate can be easily obtained.

This work comes within the scope of the following larger perspective: integrating a fuel cell in the hydrogen process. In this context, the design of the PID control laws must take into account the operating conditions of the fuel cell according to its hydrogen consumption. Notice that the proposed approach to PID design is well adapted to the changes in the operating conditions:

- first, the interesting operating conditions can be selected by studying the whole process composed by the fuel cell and PEMEL,
- second, for each selected operating condition, a model of the PEMEL can be determined using the methodology developed in Section 2.2, and the step by step PID design method presented in Section 4.3.1 can be used to design a PID controller,
- third, a gain scheduling procedure can be used to associate each designed PID to a given operating point.

As can be seen in the experimental test bench Figure 17, a RES has not been considered as power source. However, a photovoltaic power source can be used since the considered input DC voltage to supply the SIBC is low (around 30 V). For this application, the variations of the input DC voltage are small (around 8 to 10 V) depending on the weather conditions. In comparison, when considering a wind turbine as power source, the input DC voltage is higher (around a hundred volts) and the voltage variations are more important. So, the wind turbine is not suitable within the framework of this work. In addition, our approach is well adapted to take into account small variations and disturbances due to changes in weather conditions. Indeed, PID control allows to compensate disturbances effects on the steady-state error and changes in the operating conditions (see in Table 4, the role of the derivative action on overshoot and stability margin, and the effect of the integral action on the steady-state error). In addition, as above-mentioned, a gain scheduling procedure is perfectly fit with our approach to meet operating condition changes.

# References


[1] M. Kabalo, B. Blunier, D. Bouquain, A. Miraoui, State-of-the-art of DC-DC converters for fuel cell vehicles, in: Proc. IEEE Vehicle Power and Propulsion Conf., Lille, France, 2010.

[2] US Department of Energy, Fuel Cell Technologies Office, Annual Merit Review Proceedings, available under https://www.hydrogen.energy.gov/annual_review16_proceedings.html (2016).

[3] S. Koohi-Fayegh, M. Rosen, A review of energy storage types, applications and recent developments, J. of Energy Storage 27 (2020) ID 101047.

[4] S. Hajiaghasi, A. Salemnia, M. Hamzeh, Hybrid energy storage system for microgrids applications: a review, J. of Energy Storage 21 (2019) 543–570.

[5] A. Ursua, L. Gandia, P. Sanchis, Hydrogen production from water electrolysis: current status and future trends, Proceedings of the IEEE 100 (2012) 410–426.

[6] J. Koponen, Review of Water Electrolysis Technologies and Design of Renewable Hydrogen Production Systems, Master's Thesis, LUT School of Energy Systems, Lappeenranta University of Technology, Lappeenranta, Finland (2015).

[7] International Energy Agency, Technology Roadmap: Hydrogen and Fuel Cells, available under https://www.iea.org/reports/technology-roadmap-hydrogen-and-fuel-cells (2015).

[8] M. David, C. Ocampo-Martínez, R. Sánchez-Peña, Advances in alkaline water electrolyzers: a review, J. of Energy Storage 23 (2019) 392–403.

[9] M. Carmo, D. Fritz, D. S. J. Mergel a, A comprehensive review on PEM water electrolysis, Int. J. of Hydrogen Energy 38 (2013) 4901–4934.

[10] M. Blal, A. Belasri, A. Benatillah, Using the hydrogen for sustainable energy storage: designs, modeling, identification and simulation membrane behavior in PEM system electrolyser, J. of Energy Storage 7 (2016) 270–285.

[11] M. Laguna-Bercero, Recent advances in high temperature electrolysis using solid oxide fuel cells: a review, J. of Power Sources 203 (2012) 4–16.

[12] P. Olivier, C. Bourasseau, B. Bouamama, Low-temperature electrolysis system modelling: A review, Renewable and Sustainable Energy Reviews 78 (2017) 280–300.

[13] S. Collura, D. Guilbert, G. Vitale, M. Luna, F. Alonge, F. D'Ippolito, A. Scipioni, Design and experimental validation of a high voltage ratio DC/DC converter for proton exchange membrane electrolyzer applications, Int. J. of Hydrogen Energy 44 (2019) 7059–7072.

[14] M. Şahin, An efficient solar-hydrogen DC-DC buck converter system with sliding mode control, El-Cezeri Journal of Science and Engineering 6 (2019) 558–570.

[15] M. Şahin, A photovoltaic powered electrolysis converter system with maximum power point tracking control, Int. J. of Hydrogen Energy 45 (2020) 9293–9304.

[16] M. Şahin, H. Okumuş, Fuzzy logic controlled parallel connected synchronous buck DC-DC converter for water electrolysis, IETE Journal of Research 59 (2013) 280–288.

[17] D. Guilbert, S. Collura, A. Scipioni, DC/DC converter topologies for electrolyzers: state-of- the-art and remaining key issues, Int. J. of Hydrogen Energy 42 (2017) 23966–23985.

[18] M. Şahin, H. Okumuş, M. Aydemiri, Implementation of an electrolysis system with DC/DC synchronous buck converter, Int. J. of Hydrogen Energy 39 (2014) 6802–6812.

[19] P. Chandrasekhar, S. Reddy, Performance of soft-switched DC-DC resonant converter for electrolyzer, in: Proc. IEEE Int. Symp. Resilient Control Systems, Boise, USA, 2011.

[20] D. Gautam, A. Bhat, A comparison of soft-switched DC-to-DC converters for electrolyzer application, IEEE Trans. Power Electronics 28 (2013) 54–63.

[21] P. Chandrasekhar, S. Reddy, Design of LCL resonant converter for electrolyser, The Annals of "Dunarea de Jos" University of Galati Fascicle III 33 (2010) 5–11.

[22] A. Blinov, A. Andrijanovits, New DC/DC converter for electrolyser interfacing with stand-alone renewable energy system, Electrical, Control and Communication Engineering 1 (2012) 24–29.

[23] A. Andrijanovits, I. Steiks, J. Zakis, D. Vinnikov, Analysis of state-of-the-art converter topologies for interfacing of hydrogen buffer with renewable energy systems, Sci. J. of Riga Technical University 29 (2011) 87–94.

[24] A. Andrijanovits, D. Vinnikov, I. Roasto, A. Blinov, Three-level half-bridge ZVS DC/DC converter for electrolyzer integration with renewable energy systems, in: Proc. IEEE Int. Conf. on Environment and Electrical Engineering, Rome, Italy, 2011.

[25] C. Cavallaro, F. Chimento, S. Musumeci, C. Sapuppo, C. Santonocito, Electrolyser in H2 self-producing systems connected to DC link with dedicated phase shift converter, in: Proc. IEEE Int. Conf. on Clean Electrical Power, Capri, Italy, 2007.

[26] J. Monroy-Morales, M. Hernández-Ángeles, D. Campos-Gaona, R. Peña-Alzola, M. Ordonez, W. Mérida, Modeling and control design of a vienna rectifier based electrolyzer, in: Proc. IEEE Int. Symp. on Power Electronics for Distributed Generation Systems, Vancouver, Canada, 2016.

[27] R. Pittini, Z. Zhang, M. Andersen, Isolated full bridge boost DC-DC converter designed for bidirectional operation of fuel cells/electrolyzer cells in grid-tie applications, in: Proc. European Conf. on Power Electronics and Applications, Lille, France, 2013.

[28] J. Jacobs, DC/DC Converter for a Small Scale Wind Hydrogen System, Master of Thesis, Faculty of the Graduate College, University of Nebraska, Loncon, USA (2010).

[29] M. Koundi, H. El Fadil, Mathematical modeling of PEM electrolyzer and design of a voltage controller by the SMPWM approach, in: Proc. IEEE Int. Conf. on Power Generation Systems and Renewable Energy Technologies, Istanbul, Turkey, 2019.

[30] R. Miftakhutdinov, Optimal design of interleaved synchronous buck converter at high slew-rate load current transients, in: Proc. IEEE Power Electronics Specialists Conf., Vancouver, Canada, 2001.

[31] S. Somkun, C. Sirisamphanwong, S. Sukchai, Design and implementation of an interleaved boost DC-DC converter for PEM fuel cells, Applied Mechanics & Materials 666 (2014) 87–92.

[32] B. Yodwong, D. Guilbert, W. Kaewmanee, M. Phattanasak, Energy efficiency based control strategy of a three-level interleaved DC-DC buck converter supplying a proton exchange membrane electrolyzer, Electronics 8 (2019) ID 933.

[33] V. Guida, D. Guilbert, G. Vitale, B. Douine, Design and realization of a stacked interleaved DC-DC step-down converter for PEM water electrolysis with improved current control, Fuel Cells 20 (2020) 307–315.

[34] D. Guilbert, D. Sorbera, G. Vitale, A stacked interleaved DC-DC buck converter for proton exchange membrane electrolyzer applications: Design and experimental validation, Int. J. of Hydrogen Energy 45 (2020) 64–69.

[35] D. Guilbert, G. Vitale, Dynamic emulation of a PEM electrolyzer by time constant based exponential model, Energies 12 (2019) ID 750.

[36] R. Middlebrook, S. Cuk, A general unified approach to modelling switching-converter power stages, in: Proc. IEEE Power Electronics Specialists Conf., Cleveland, USA, 1976.

[37] N. Mohan, T. Undeland, W. Robbins, Power Electronics, 2nd Edition, Wiley, New York, 1995.

[38] O. Alavi, A. Hooshmand-Viki, M. Bina, M. Akbari, Reliability assessment of a stand-alone wind-hydrogen energy conversion system based on thermal analysis, Int. J. of Hydrogen Energy 42 (2017) 14968–14979.

[39] S. Zorica, M. Vukšić, T. Betti, Design considerations of the multi-resonant converter as a constant current source for electrolyser utilisation, Int. J. of Electrical Power & Energy Systems 111 (2019) 237–247.

[40] M. Albarghot, L. Rolland, Comparison of experimental results with simulation of a PEM electrolyzer powered by a horizontal wind turbine, in: Proc. IEEE Int. Conf. Electrical and Electronic Technologies for Automotive, Torino, Italy, 2017.

[41] O. Atlam, An experimental and modelling study of a photovoltaic/proton-exchange membrane electrolyser system, Int. J. of Hydrogen Energy 34 (2009) 6589–6595.

[42] O. Atlam, M. Kolhe, Equivalent electrical model for a proton exchange membrane (PEM) electrolyser, Energy Conversion and Management 52 (2011) 2952–2957.

[43] S. Muyeen, R. Takahashi, J. Tamura, Electrolyzer switching strategy for hydrogen generation from variable speed wind generator, Electric Power Systems Research 81 (2011) 1171–1179.

[44] F. da Costa Lopes, E. Watanabe, Experimental and theoretical development of a pem electrolyzer model applied to energy storage systems, in: Proc. Brazilian Power Electronics Conf., Bonito-Mato Grosso do Sul, Brazil, 2009.

[45] P. Ayivor, J. Torres, M. van der Meijden, R. van der Pluijm, B. Stouwie, Modelling of large size electrolyzer for electrical grid stability studies in real time digital simulation, in: Proc. Int. Hybrid Power Systems Workshop, Tenerife, Spain, 2018.

[46] F. Speckmann, S. Bintz, K. Birke, Influence of rectifiers on the energy demand and gas quality of alkaline electrolysis systems in dynamic operation, Applied Energy 250 (2019) 855–863.

[47] B. Moore, Principal component analysis in linear systems: controllability, observability, and model reduction, IEEE Trans. Aut. Control 26 (1981) 17–32.

[48] J. Wibben, R. Harjanii, A high-efficiency DC-DC converter using 2 nH integrated inductors, IEEE J. of Solid-State Circuits 43 (2008) 844–854.

[49] K. Åström, T. Hägglund, PID Controllers: Theory, Design and Tuning, 2nd Edition, Instrument Society of America, Research Triangle Park, 1995.

[50] M. Unar, D. Murray-Smith, S. Shah, Design and tuning of fixed structure PID controllers: a survey, Tech. Rep. CSC 96016, University of Glasgow, Glasgow, UK (1996).

[51] G. van der Zalm, Tuning of PID-type controllers: literature overview, Tech. Rep. DCT 2004.54, Technical University of Eindhoven, Eindhoven, The Netherlands (2004).

[52] Y. Li, K. Ang, G. Chong, PID control system analysis and design: problems, remedies, and future directions, IEEE Contr. Syst. Magazine 26 (1) (2006) 32–41.

[53] J. Ziegler, N. Nichols, Optimum settings for automatic controllers, Trans. of the ASME 64 (1942) 759–768.

[54] J. H. K.L. Chien and, J. Reswick, On the automatic control of generalized passive systems, Trans. of the ASME 74 (1952) 175–185.

[55] G. Cohen, G. Coon, Theoretical considerations of retarded control, Trans. of the ASME 75 (1953) 827–834.

[56] P. Prouvost, Instrumentation et Régulation en 30 Fiches, Dunod, Paris, 2010.

[57] M. Zasadzinski, Régulateurs PID, Lecture Notes, IUT, dpt. GEII, Université de Lorraine, Longwy, France (2017).

[58] K. Åström, T. Hägglund, Automatic tuning of simple regulators with specifications on phase and amplitude margins, Automatica 20 (1984) 645–651.

Table 7: Nomenclature.

| **Acronyms** | |
|---|---|
| IGBT | Insulated Gate Bipolar Transistor |
| PEMEL | Proton Exchange Membrane Electrolyzer |
| PI | Proportional and Integral |
| PID | Proportional, Integral and Derivative |
| PWM | Pulse Width Modulation |
| RES | Renewable Energy Sources |
| SIBC | Stacked Interleaved DC-DC Buck Converter |
| **Roman Symbols** | |
| $A$, $B$, $C$ | Matrices of the state-space realization of the SIBC+PEMEL model |
| $C_1(s)$, $C_2(s)$, $C_3(s)$ | PID controllers |
| $C_a$ | Capacitor in PEMEL model |
| $C_p$ | First phase capacitor |
| $C_s$ | Second phase capacitor |
| $D$ | Duty cycle |
| $\overline{D}_h(z)$ | Denominator of $\overline{F}_h(z)$ |
| $e$ | Closed loop error in PID control |
| $F_h(s)$ | Continuous-time transfer function of PEMEL |
| $\overline{F}_h(s)$ | Discrete-time transfer function of PEMEL before truncation |
| $\widetilde{F}_h(s)$ | Continuous-time transfer function of PEMEL before truncation |
| $F_{h_1}(s)$, $F_{h_2}(s)$, $F_{h_3}(s)$ | $F_h(s)$ for $n_r = 1$, $n_r = 2$ and $n_r = 3$ |
| $G(s)$ | Transfer function vector of the SIBC+PEMEL model |
| $G_i(s)$ | $1^{\text{st}}$ component of vector $G(s) \rightarrow$ current |
| $G_v(s)$ | $2^{\text{nd}}$ component of vector $G(s) \rightarrow$ voltage |
| $h_1$ to $h_8$ | Hankel singular values of $\widetilde{F}_h(s)$ |
| $i_{e\ell}$ | PEMEL current |
| $i_p$ | First phase current |
| $i_s$ | Second phase current |
| $j$ | Imaginary unit of a complex number |
| $k_h$ | Steady-state gain of the PEMEL model |
| $k_i$ | Steady-state gain of $G_i(s)$ |
| $K_{\text{osc}}$ | Critical gain |
| $K_{\text{osc}_i}$, $K_{\text{osc}_v}$ | Critical gains for $G_i(s)$ and $G_v(s)$ |
| $K_p$ | Proportional gain of the PID controller |
| $k_v$ | Steady-state gain of $G_v(s)$ |
| $L_p$ | First phase inductor |
| $L_s$ | Second phase inductor |
| $m_i$ | Peak of the magnitude of $G_i(s)$ |
| $m_v$ | Peak of the magnitude of $Gv(s)$ |
| $N$ | Filtering ratio of the PID controller |
| $n$ | Order of $\overline{F}_h(z)$ and $\widetilde{F}_h(s)$ |
| $\mathcal{N}$ | Number of available samplings in Figure 3 |
| $\overline{N}_h(z)$ | Numerator of $\overline{F}_h(z)$ |
| $n_r$ | Order of $F_h(s)$ |
| $p_1$ to $p_5$ | poles of $G(s)$, so also for $G_i(s)$ and $G_v(s)$ |
| $r$ | Reference signal for PID control |
| $R_a$ | Resistor in PEMEL model |
| $R_b$ | Resistor in PEMEL model |
| $R_{\ell p}$ | Parasitic resistor of the inductor $L_p$ |
| $R_{\ell s}$ | Parasitic resistor of the inductor $L_s$ |

Table 7: Nomenclature (continued).

| **Roman Symbols** | |
|---|---|
| $T_1$, $T_{2_1}$, $T_{3_1}$, $T_{3_2}$, $T_{3_3}$ | Time constants of $F_{h_1}(s)$, $F_{h_2}(s)$ and $F_{h_3}(s)$ |
| $T_1$ to $T_4$ | Time constants of of $G(s)$ |
| $\mathcal{T}_1$ to $\mathcal{T}_4$ | Power switches of the SIBC |
| $T_c$ | Switching period of the SIBC |
| $T_d$ | Derivative time constant of the PID controller |
| $T_i$ | Integral time constant of the PID controller |
| $T_{\text{osc}}$ | Ultimate period |
| $T_s$ | Sample time interval |
| $t_s$ | Settling time of $G(s)$ |
| $u$ | Control input of the state-space realization of the SIBC+PEMEL model |
| $v_{ca}$ | Voltage at the terminals of capacitor $C_a$ |
| $v_{cs}$ | Voltage at the terminals of capacitor $C_s$ |
| $v_{e\ell}$ | PEMEL voltage |
| $V_i$ | Input voltage of the SIBC |
| $V_{\text{int}}$ | Reversible voltage in PEMEL model |
| $x$ | State of the state-space realization of the SIBC+PEMEL model |
| $x_h$ | State of the state-space realization of the PEMEL model |
| $y$ | Measured output of the state-space realization of the SIBC+PEMEL model |
| $\overline{y}$ | Measurement in PID control (either $i_{e\ell}$ or $v_{e\ell}$) |
| $Y_{\mathcal{N}}$ | Vector of measured outputs |
| $z_i$ | Zero of $G_i(s)$ |
| $z_v$ | Zero of $G_v(s)$ |
| **Greek Symbols** | |
| $\alpha$ | Ratio between $T_i$ and $T_d$ in PID $C_3(s)$ |
| $\varepsilon_k$ | Modeling error |
| $\mathcal{E}_{\mathcal{N}}$ | Vector of modeling errors in least-square procedure |
| $\zeta$ | Damping factor of $G(s)$ |
| $\theta$ | Vector of coefficients of $\overline{F}_h(z)$ |
| $\widehat{\theta}$ | Vector of estimated coefficients of $\overline{F}_h(z)$ |
| $\tau_d$ | Filter time constant of the PID controller |
| $\phi_m$ | Desired phase margin |
| $\Phi_{\mathcal{N}}$ | Regression matrix |
| $\omega$ | Frequency in rad/s |
| $\omega_c$ | Switching frequency of the SIBC (rad/s) |
| $\omega_n$ | Natural frequency of $G(s)$ |
| $\omega_p$ | Frequency at the peak of the magnitude of $G_i(s)$ and $G_v(s)$ (rad/s) |